Volume 2

Application of relations between seismic amplitude, velocity and lithology in geological interpretation of seismic data

Smiljan Prskalo[1]

1INA d.d Naftaplin, Zagreb, Croatia, E-mail: sprskalo@ina.hr

Abstract

Geological interpretation of seismic data should fulfill two main objectives: solving geometry of structures with possible hydrocarbon accumulations and correlation of recorded seismic amplitudes and velocities with lithology. The first objective is easily achieved through already well established procedures of structural interpretation, while the second one is still based on factors highly depending on interpreters' previous experiences. In order to establish some reliable criteria for interpretation lithology and fluid saturation of possible interesting reservoir rocks, relation between physical rock properties (density, elasticity, fluid saturation) and seismic waves velocity and amplitudes were already analyzed and presented in many so far publicized works. According to them seismic velocities depend on rock elasticity and density, i.e. on rock lithology. As the reflected seismic wave amplitudes are functions of acoustic impedances – product of velocity and density – therefore they can be interpreted in terms of rock properties (lithology, fluid type and saturation), and even used as direct hydrocarbon indicators.

In the article mathematical relations between elasticity, velocity and amplitude are presented according to the known, already publicized works listed in Reference. Short description of physical meaning of these formulae, as well as discussion of their practical applications, is done in the next part. Finally, some examples of hydrocarbon – particularly gas – reservoir exploration on Adriatic Sea are presented in order to illustrate real possibilities of this approach to seismic data interpretation.

Keywords: seismic, amplitude, velocity, geological interpretation, Adriatic Sea

INTRODUCTION

The main objective of seismic data application in hydrocarbon exploration has not been changed during the last 40 years. At the same time the technology of seismic methods has drastically improved and enabled exploration geophycists to meet many times higher demands involving seismic methods in every day use in reservoir exploration and development.

Oil and gas accumulations could be formed in structural and stratigraphic traps. The definition of underground geometry is based on the times needed for seismic wave to travel the path source – reflector – receiver. The procedure of structural interpretation is today well established, relatively not very demanding procedure, highly performed using powerful computers. In other words, following certain rules concerning seismic reflections picking on the properly processed 2D or 3D data presentations, and their correlation with well data, a reliable geological model of the explored underground could be established.
The first attempts of solving lithology and oil and gas finding by seismic methods are connected with the commencement of seismic methods practical applications. Due to the fact that these tasks can be solved by analyzing seismic wave characteristics (amplitude, frequency, polarity, velocity) using seismic data of excellent quality, such information became available only after successful advances in seismic technology. However, seismic amplitudes analysis in at least qualitative lithology determinations, were practically used all the time, in spite to the lack of publicized works, mainly due to keeping such procedures as big companies' secrets.
Theoretical background for seismic amplitude interpretation, necessary in recently developed AVO (Amplitude-Versus-Offset) method has been already established at the beginning of the last century. In the Knott's and Zoeppritz's works (Knott, 1899, Zoeppritz, 1919) the seismic amplitude dependence on seismic velocity and density in two layer medium were analyzed. Based on these works, equations describing amplitude changes as functions of P and S wave velocities, density and angle of incidence of seismic arrival on the reflector, were developed. These equations were rather very complex and therefore it was very difficult, practically almost impossible, to find their solutions.
During later years it was attempted to simplify them in order to make them usable in practice. Petrophysical link to seismic data was described by Gassmann (Gassmann, 1951) in his 1951 article. In this article, publicized in 1955, Koefoed (Koefoed, 1955) presented an expression describing offset dependent amplitude change and established theoretical background for in the future very popular AVO method. The first systematic attempt in lithology prognosis through reflection coefficients analysis was described by Rosa (Rosa, 1976). Further development in practical use of amplitudes in lithology and fluid saturation is connected with the works of Ostrander (Ostrander, 1982 and 1984). In the 1985 Shuey (Shuey, 1985) publicized the article on linear approximation equation later widely used in practical application of AVO method.

SEISMIC VELOCITIES VERSUS ROCK PHYSICS

Force impulse acting on the surface results in spreading volume P and S wave along rays starting in the seismic source. Seismic wave fronts in the homogeneous medium are symmetric spheres with curvatures continuously increasing as the distance from the source increases. At the very long distance (theoretically close to infinity) the wave fronts became planes, and rays linear. These approximations are used in the following derivations. Accordingly, seismic velocities change only at the reflecting surfaces between two media (layers), making easier further theoretical analysis.
Under the stress, the observed point moves from its original position $\mathbf{P}(x_0, y_0, z_0)$ to the new position $\mathbf{P}(x_0+\Delta x, y_0+\Delta y, z_0+\Delta z)$ in Cartesian coordinates, as shown on ***Fig.1.*** Resulting shifts in the 3 directions, shown on the figure are defined as $\Delta x = u$, $\Delta y = v$ and $\Delta z = w$.
The linear strains ε_{xx}, ε_{yy}, ε_{zz} in the ***x, y*** and ***z*** directions are equal to the changes in lengths per unit lengths defined by expressions

$$\varepsilon_{xx} = \frac{\partial u}{\partial x}, \quad \varepsilon_{yy} = \frac{\partial v}{\partial y}, \quad \varepsilon_{zz} = \frac{\partial w}{\partial z} \tag{1}$$

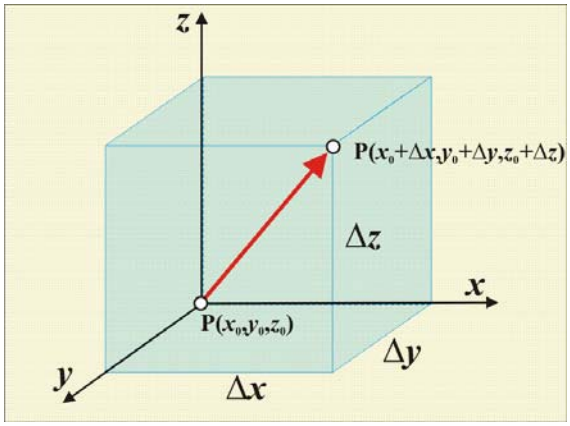

Fig.1: Point position change under stress

Volume strain, θ, or dilatation is the change in volume per unit volume, defined by

$$\theta = \frac{\partial u}{\partial x} + \frac{\partial v}{\partial y} + \frac{\partial w}{\partial z} = \varepsilon_{xx} + \varepsilon_{yy} + \varepsilon_{zz} \tag{2}$$

The ratio of lateral contraction to linear extension in a strained element is Poisson ratio. Such extension in the ***x***-direction is defined by following relations

$$\sigma = \frac{\partial v/\partial y}{\partial u/\partial x} = \frac{\varepsilon_{yy}}{\varepsilon_{xx}}$$
$$\sigma = \frac{\partial w/\partial z}{\partial u/\partial x} = \frac{\varepsilon_{zz}}{\varepsilon_{xx}} \tag{3}$$

Stress is defined as the ratio of force to area, in the limit, as the area approaches zero value. On ***Fig. 2*** components of stress acting in the ***x***, ***y*** and ***z*** directions are shown.

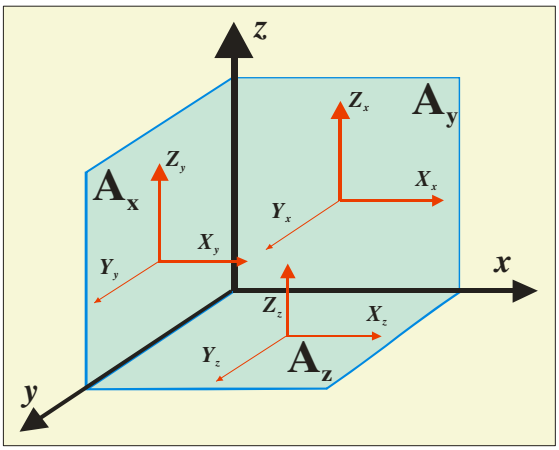

Fig.2: Stress components

The nine components of stress, X_x, X_y, X_z, Y_x, Y_y, Y_z, Z_x, Z_y, Z_z, are shown on the figure. The capital letter indicates the direction of stress and the subscript indicates the direction of the normal to the surface. To maintain equilibrium, the components of shear stress must satisfy relations:

$$X_y = Y_x, \quad X_z = Z_x, \quad Y_z = Z_y \tag{4}$$

With the 3 compress ional stress components X_x, Y_y and Z_z they form a total of six independent stress components. According to Hook's law the stress is proportional to the strain. In general, each of the six independent components of stress at a point (X_x, Y_y, Z_z, X_y, X_z, Y_z) is linear functions of the six independent components of strain (ε_{xx}, ε_{yy}, ε_{zz}, ε_{xy}, ε_{yz}, ε_{zx}). This results in 36 elastic constants, 21 of which are independent if no symmetry exists. In a homogeneous and isotropic material, the number of independent elastic constants is reduced to the Lame constants, λ and μ, and stress-strain relations become

$$\begin{aligned} &X_x = \lambda\theta + 2\mu\varepsilon_{xx}, \quad Y_y = \lambda\theta + 2\mu\varepsilon_{yy}, \quad Z_y = \lambda\theta + 2\mu\varepsilon_{zz}, \quad and \\ &X_y = Y_x = \mu\varepsilon_{xy} = \mu\varepsilon_{yx}, \quad X_z = Z_x = \mu\varepsilon_{xz} = \mu\varepsilon_{zx}, \quad Y_z = Z_y = \mu\varepsilon_{yz} = \mu\varepsilon_{zy} \end{aligned} \tag{5}$$

In the case of purely compressional stress applied in the x-direction when all other stress components are equal to zero, and after substituting θ with right hand side of equation (2), the first three equations in (5) became

$$\begin{aligned} X_x &= (\lambda + 2\mu)\cdot\varepsilon_{xx} + \lambda\cdot(\varepsilon_{yy} + \varepsilon_{zz}) \\ 0 &= (\lambda + 2\mu)\cdot\varepsilon_{yy} + \lambda\cdot(\varepsilon_{xx} + \varepsilon_{zz}) \\ 0 &= (\lambda + 2\mu)\cdot\varepsilon_{zz} + \lambda\cdot(\varepsilon_{xx} + \varepsilon_{yy}) \end{aligned} \tag{6}$$

Solving for ε_{xx}, ε_{yy}, ε_{zz} gives

$$\varepsilon_{xx} = \frac{\lambda + \mu}{\mu(3\lambda + 2\mu)}\cdot X_x \qquad and \qquad \varepsilon_{yy} = \varepsilon_{zz} = \frac{\lambda}{2\mu(3\lambda + 2\mu)}\cdot X_x \tag{7}$$

Young's modulus E, and Poisson's ratio σ, shown on ***Fig.3***, are defined as follows

$$\begin{aligned} E &= \frac{X_x}{\varepsilon_{xx}} = \frac{\mu(3\lambda + 2\mu)}{\lambda + \mu} = \frac{F/A}{\Delta L/L} \quad i \\ \sigma &= \frac{\varepsilon_{yy}}{\varepsilon_{xx}} = \frac{\lambda}{2(\lambda + \mu)} = \frac{\Delta D/D}{\Delta L/L} \end{aligned} \tag{8}$$

Under uniform hydrostatic pressure on the unit sphere normal stress components X_x, Y_y and Z_z are equal to the pressure P, while the shear stress components became 0. According to this, stress-strain relation is defined by

$$\varepsilon_{xx} = \varepsilon_{yy} = \varepsilon_{zz} = -\frac{P}{3\lambda + 2\mu} \tag{9}$$

Volume change $\theta = \Delta Vol/Vol$ defines bulk modulus k according to the relation

$$k = \frac{P}{\theta} = \frac{P}{\varepsilon_{xx} + \varepsilon_{yy} + \varepsilon_{zz}} = \lambda + \frac{2}{3}\mu = \frac{P}{\Delta Vol/Vol} \tag{10}$$

Seismic wave arrival on the side of unit cube with the angle different from 90^0, as shown in lower right angle of ***Fig. 3***, causes shear defined by elastic shear modulus μ depending on the stress F/A and the length of cube's side $\Delta D/D$, according to the following relation

$$\mu = \frac{\tau}{tg\,\phi} = \frac{F/A}{\Delta D/D} \tag{11}$$

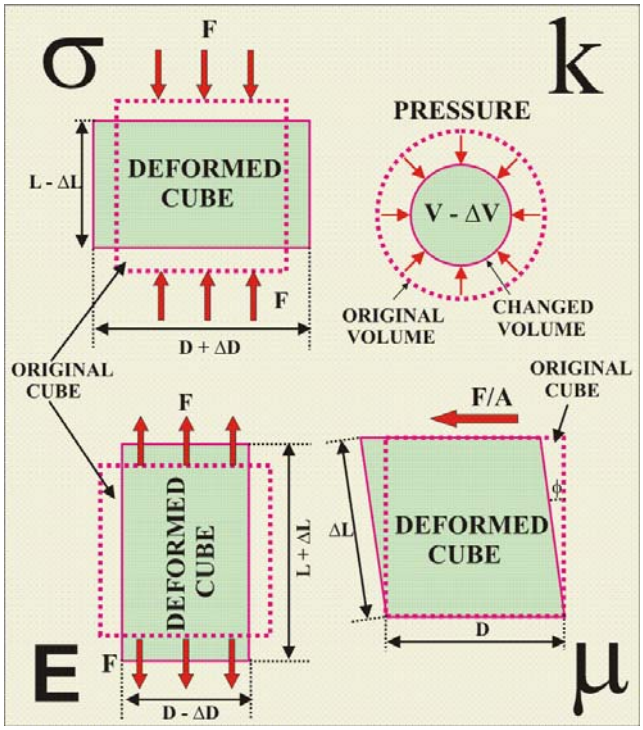

Fig.3: Elastic constants

After combining the above relations Lame's constant λ is derived as

$$\lambda = \frac{\sigma \cdot E}{(1+\sigma)\cdot(1-2\sigma)} \qquad (12)$$

According to the relations shown on ***Fig.4***, the difference between components of X_x stress acting on opposite **ABCD** and **EFGH** sides, is defined as follows

$$\left(X_x + \frac{\partial X_x}{\partial x}\Delta x\right) - X_x = \frac{\partial X_x}{\partial x}\Delta x \qquad (13)$$

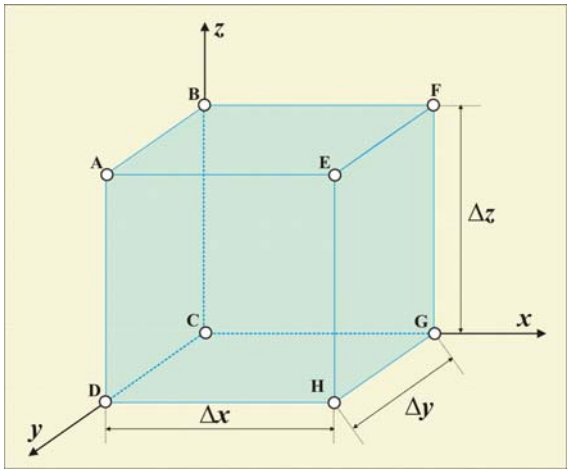

Fig.4: Stress acting on the unit cube

Resulting force F_x is equal to the stress X_x multiplied with the surface area $\Delta y \Delta z$ on which it is acting, i.e.:

$$F_x = \left(\frac{\partial X_x}{\partial x} \Delta x \right) \cdot (\Delta y \Delta z) \tag{14}$$

The forces, F_y and F_z, acting on the other two sides are

$$F_y = \left(\frac{\partial X_y}{\partial y} \Delta y \right) \cdot (\Delta x \Delta z), \qquad F_z = \left(\frac{\partial X_z}{\partial z} \Delta z \right) \cdot (\Delta x \Delta y) \tag{15}$$

According to the second Newton's law $F_x = ma_x$, after mass m is replaced by product of density ρ and change of volume $\rho \Delta x \Delta y \Delta z$, and acceleration a_x with the second partial derivation of shift u per time t, the following relation is obtained

$$F_x = ma_x \rightarrow \left(\frac{\partial X_x}{\partial x} + \frac{\partial X_y}{\partial y} + \frac{\partial X_z}{\partial z} \right) = \rho \frac{\partial^2 u}{\partial t^2} \tag{16}$$

The expressions for forces F_y and F_z, acting in the other two directions are similar. Obviously in them only need to replace the shift u on the right hand side of the equation with v or w.

In the homogeneous isotropic medium, after introducing elastic constants, the above equations became

$$\begin{aligned}
(\lambda + \mu) \frac{\partial \theta}{\partial x} + \mu \left(\frac{\partial^2 u}{\partial x^2} + \frac{\partial^2 u}{\partial y^2} + \frac{\partial^2 u}{\partial z^2} \right) &= \rho \frac{\partial^2 u}{\partial t^2} \\
(\lambda + \mu) \frac{\partial \theta}{\partial y} + \mu \left(\frac{\partial^2 v}{\partial x^2} + \frac{\partial^2 v}{\partial y^2} + \frac{\partial^2 v}{\partial z^2} \right) &= \rho \frac{\partial^2 v}{\partial t^2} \\
(\lambda + \mu) \frac{\partial \theta}{\partial z} + \mu \left(\frac{\partial^2 w}{\partial x^2} + \frac{\partial^2 w}{\partial y^2} + \frac{\partial^2 w}{\partial z^2} \right) &= \rho \frac{\partial^2 w}{\partial t^2}
\end{aligned} \tag{17}$$

For the plane wave spreading only in x-direction, all members with partial derivation in y and z directions are equal to 0, and the partial derivation of change θ per unit distance in x-direction is equal to the following relation

$$\frac{\partial \theta}{\partial x} = \frac{\partial^2 u}{\partial x^2} \tag{18}$$

The final equations describing plane wave spreading became as follows

$$\begin{aligned}
\frac{\partial^2 u}{\partial t^2} &= \frac{\lambda + 2\mu}{\rho} \cdot \frac{\partial^2 u}{\partial x^2}, \\
\frac{\partial^2 v}{\partial t^2} &= \frac{\mu}{\rho} \cdot \frac{\partial^2 v}{\partial x^2}, \\
\frac{\partial^2 w}{\partial t^2} &= \frac{\mu}{\rho} \cdot \frac{\partial^2 w}{\partial x^2}
\end{aligned} \tag{19}$$

The first equation in the relation (19) defines P-wave velocity V_P

$$V_P = \sqrt{\frac{k + 4\mu/3}{\rho}} = \sqrt{\frac{\lambda + 2\mu}{\rho}} \tag{20}$$

and the two following S-wave velocity, V_S, in the homogeneous media

$$V_S = \sqrt{\frac{\mu}{\rho}} \tag{21}$$

In the water, as well as other fluids, only ***P***-waves are spreading. The acoustic wave arrival causes pressure increase which forces movements of the water molecules toward each other. Intermolecular forces try to prevent such movements and move the molecules to their original locations. The final result of these opposite forces is seismic wave which is spreading only along the pressure increase direction only as ***P***-wave. In other words in fluids shear modulus μ is equal to 0, and the velocities of ***P*** and ***S*** waves are defined as follows

$$V_P = \sqrt{\frac{k}{\rho}} \qquad V_s = 0 \tag{22}$$

The results of the calculations ***P*** and ***S*** wave velocity, performed using the above equations, are shown on ***Fig.5***. Poisson's ratio s, rewritten in the form

$$\sigma = \frac{\left[(V_P/V_S)^2 - 0{,}5\right] - 1}{(V_P/V_S)^2 - 1} \tag{23}$$

is good indicator for lithology and fluid saturation. In the liquids it is equal to 0.5, and in the ideally hard rocks 0.25. Usually this ratio has values between 0.25 and 0.35, while in the unconsolidated sediments could even increase up to 0.40 and 0.45. A change of physical rock characteristics (lithology, porosity, fluid type and saturation, pressure) results in the change of ***P*** and ***S*** wave velocity and indirectly in the change of Poisson's ratio. If, for example, water or oil in the reservoir rock is replaced with very small amount of gas (even slightly bellow 5%), ***P*** wave velocity will drastically decrease, while the ***S*** wave velocity will show rather minor change.

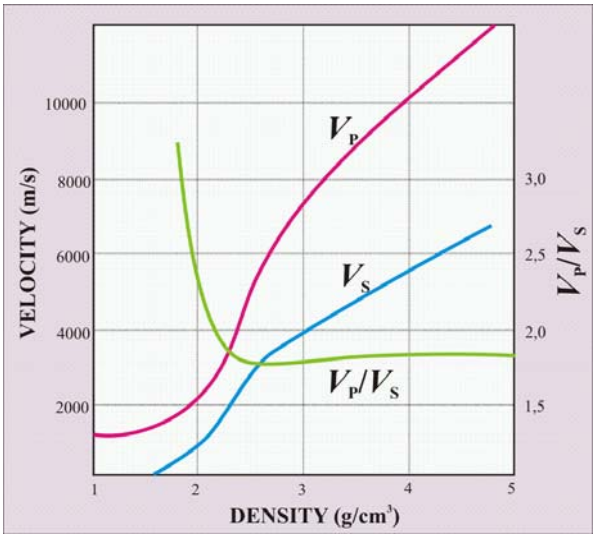

Fig.5: Relations between P wave velocity (VP), S wave velocity (VS), and their ratio (VP/VS) and density

Complex causal relations between elastic constants, density and seismic velocity according to the above equations and text obviously exist and could be successfully applied in lithology and fluid determinations on the basis of seismic data. Some of these relations are presented on ***Fig.6***. In the "soft" materials with small acoustic impedances (product velocity and density), like shale, a seismic wave arrival causes big particle movements and small pressure increase. For the "hard" materials with big acoustic impedances, like limestone, high pressure and small particle movements are characterizing seismic wave arrival.

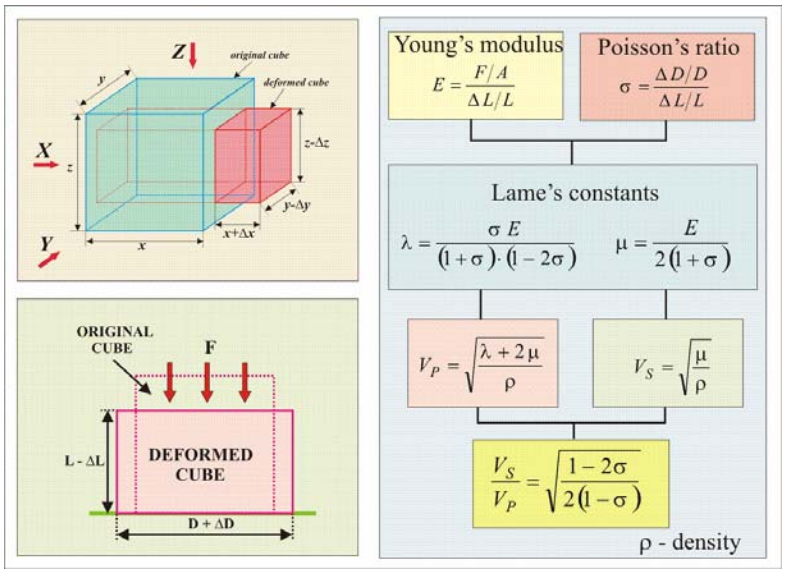

Fig.6: Relations between elastic constants and seismic velocities

Short summary of the effect of different rock properties on seismic ***P*** and ***S*** wave velocity and their ratio is presented on ***Fig.7*** (Tatham, 1991).

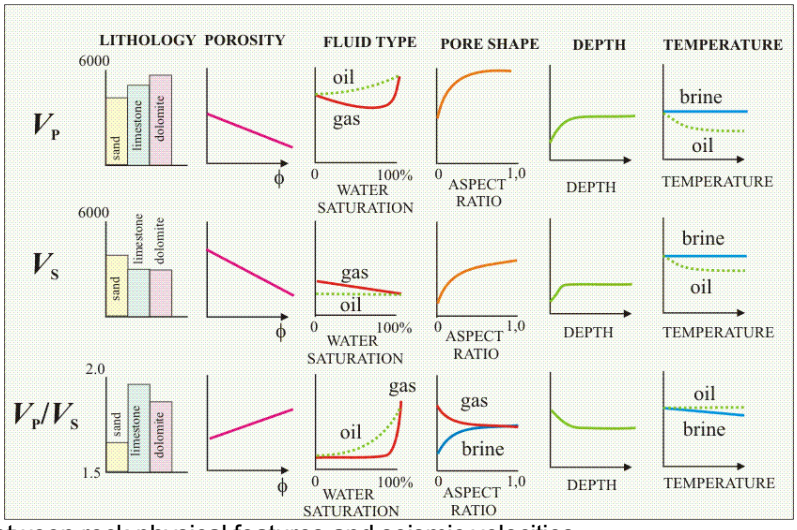

Fig.7: Relations between rock physical features and seismic velocities

Ranges of ***P*** and ***S*** waves velocities differ depending on lithology, in spite of certain overlapping, as shown on the first column on ***Fig.7***. The ***P*** wave velocity, V_P, is the highest in dolomite and the lowest in sand. Quite opposite situation is valid for ***S*** wave velocity, V_S, where the highest value is recorded in sands. As shown in the third row in the same column it has direct influence on V_P/V_S ratio. If porosity increases both velocities decrease. Faster decrease of shear wave velocity causes the increase of velocity ratio with porosity increase (the second column). Oil and gas saturations decrease, or water saturation increases, result in increase of ***P*** wave velocity, V_P, and decrease of ***S*** wave velocity, V_S, as shown in the third column. The velocity ratio, V_P/V_S, is increasing (the third row). It is important to notice that the same ratio in the gas saturated rock is constant until gas saturation became less than 5%. Increasing the aspect ratio, as shown in the fourth column, that is, more rounded pores; increase both ***P*** and ***S*** wave velocities. Increasing consolidation or depth of burial of rock increase both velocities and decrease their ratio. Temperature change causes both velocities changes only in oil saturated rocks, and very small change in velocity ratio.

AMPLITUDE VERSUS REFLECTION COEFFICIENT

Seismic waves on their way through the Earth underground change characteristics. When the seismic wave front strikes an interface, the wave is partially reflected in the first and partially transmitted into the second medium. Upon striking the interface at normal incidence, incident plane wave with unit amplitude produces reflection whose amplitude depends on acoustic impedance, i.e. on velocity-density product of each medium. Therefore the amplitude of the reflected wave is a function of the reflection coefficient, ***R***, defined by acoustic impedances, z_1 and z_2, products of densities, ρ_1 and ρ_2, and velocities, V_1 and V_2, of each medium, as follows

$$R = \frac{z_2 - z_1}{z_2 + z_1} = \frac{\rho_2 \cdot V_2 - \rho_1 \cdot V_1}{\rho_2 \cdot V_2 + \rho_1 \cdot V_1} \qquad (24)$$

The amplitude of the transmitted wave is defined by transmission coefficient which is equal to the relation

$$T = 1 - R = \frac{2 \cdot z_1}{z_2 + z_1} = \frac{2 \cdot \rho_1 \cdot V_1}{\rho_2 \cdot V_2 + \rho_1 \cdot V_1} \qquad (25)$$

As shown in the equation (25), amplitudes of reflected seismic waves are higher and have positive polarity, if the velocity is regularly increasing with depth. If the solution of the equation (25) is negative, as on the interfaces where bottom layer has lower acoustic impedance, the amplitude polarity change occurs. On the interfaces between seal rocks and reservoir gas saturated rocks very high reflected amplitudes are usually produced. The especially high reflected amplitudes, called bright spots, appear on the seismic sections recorded above gas reservoir rocks. One seismic section with this feature is shown on ***Fig.8***.

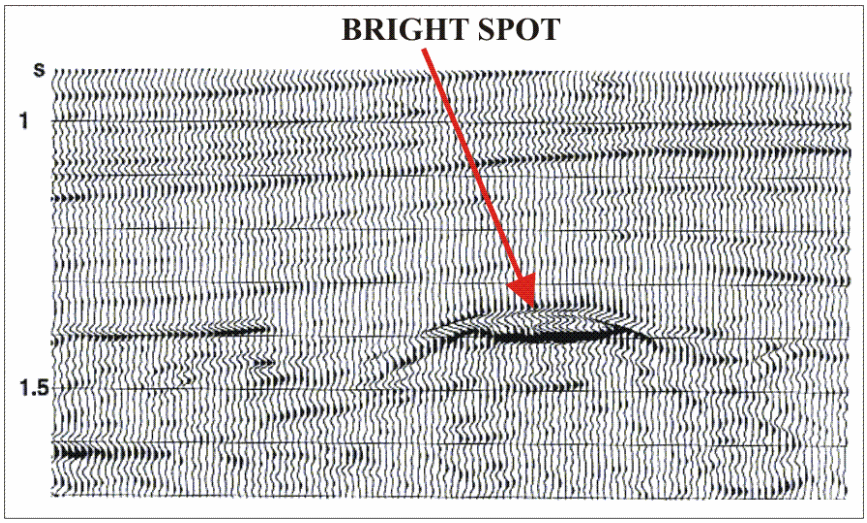

Fig.8: Bright spot effect

Every seismic wave arrival at the reflecting surface between two underground layers with an angle of incidence different from 90° results, as shown on ***Fig.9***, in the formation of four new seismic waves:

- Reflected ***P*** wave
- Reflected ***S*** wave
- Refracted ***P*** wave
- Refracted ***S*** wave

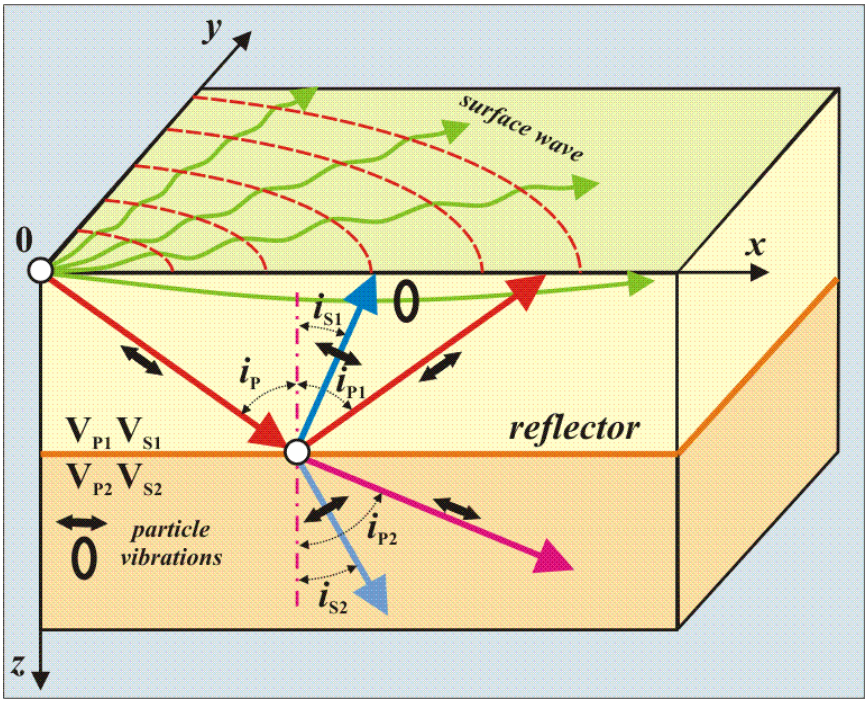

Fig.9: Seismic waves created on reflecting surface

According to Snell's low, ***P*** and ***S*** wave velocities and their angles of reflection and refraction exist following relations:

$$\frac{\sin i_p}{V_{p1}} = \frac{\sin i_{p2}}{V_{p2}} = \frac{\sin i_{s1}}{V_{s1}} = \frac{\sin i_{s2}}{V_{s2}} = p \qquad (26)$$

where

V_{p1} – ***P*** wave velocity in the upper layer
V_{p2} – ***P*** wave velocity in the lower layer
V_{s1} – ***S*** wave velocity in the upper layer
V_{s2} – ***S*** wave velocity in the lower layer
i_P – angle of incidence
i_{P1} – angle of reflection for ***P*** wave
i_{S1} – angle of reflection for ***S*** wave
i_{P2} – angle of refraction for ***P*** wave
i_{S2} – angle of refraction for ***P*** wave
p – seismic ray parameter

Seismic amplitudes, as well as their powers, are directly dependent on angles of incidence. On ***Fig.10*** normalized values of amplitude powers of reflected and transmitted ***P*** and ***S*** waves in two layer medium are shown. The ***P*** wave reflected amplitude is continually increasing as the angle of incidence increases, while the power of transmitted wave decreases and became zero at the angle of approximately 30^0. At the same angle reflected and transmitted ***S*** wave amplitudes quickly increased from zero to maximum value of 0.2 or 0.4. Further increase of the angle results in continuous decrease of both S amplitudes, and beyond the angle of 60^0 transmitted ***S*** wave ceased to exist.

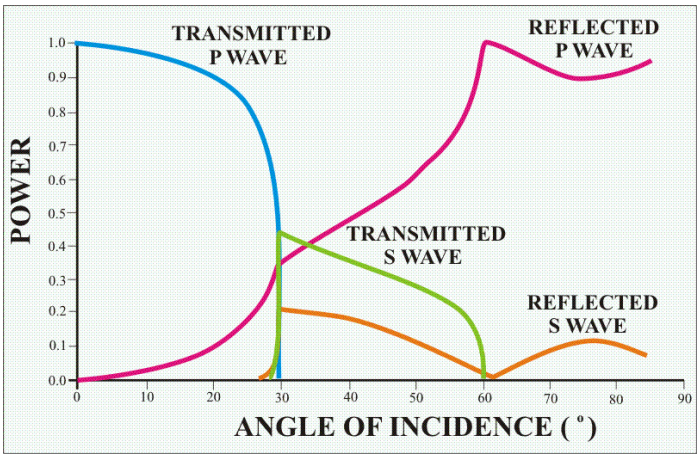

Fig.10: Amplitude vs. angle of incidence for reflected and refracted waves

By the application of Snell's low to the limiting conditions Knott-Zoepritz's equations are derived. They state that between reflection and transmission coefficients, angles of reflection and refraction, ***P*** and ***S*** wave velocities, and densities in two layers medium the following relations exist

$$(A_0 - A_1)\cdot \cos\alpha_p + B_1 \cdot \sin\alpha_s = A_2 \cdot \cos\beta_p + B_2 \cdot \sin\beta_s \qquad (27)$$

$$(A_0 + A_1)\cdot \sin\alpha_p + B_1 \cdot \cos\alpha_s = A_2 \cdot \sin\beta_p - B_2 \cdot \cos\beta_s \qquad (28)$$

$$(A_0 + A_1)\cdot \cos\alpha_s - B_1\left(\frac{V_{s1}}{V_{p1}}\right)\sin 2\beta_s = A_2\left(\frac{\rho_2 \cdot V_{p2}}{\rho_1 \cdot V_{p1}}\right)\sin 2\beta_s + B_2\left(\frac{\rho_2 \cdot V_{s2}}{\rho_1 \cdot V_{p1}}\right)\sin 2\beta_s \qquad (29)$$

$$\rho_1 V_{s1}^2\left[(A_0 - A_1)\sin 2\alpha_p - B_1\left(\frac{V_{p1}}{V_{s1}}\right)\cos 2\alpha_s\right] = \rho_2 V_{s2}^2\left[A_2\left(\frac{V_{p1}}{V_{p2}}\right)\sin 2\beta_p - B_2\left(\frac{V_{p1}}{V_{s2}}\right)\cos 2\beta_s\right] \qquad (30)$$

In the above equations the following symbols were used:

- A_0 – incident ***P*** wave amplitude
- A_1 – reflected ***P*** wave amplitude
- A_2 – refracted ***P*** wave amplitude
- B_1 – reflected ***S*** wave amplitude
- B_2 – refracted ***S*** wave amplitude
- V_{p1} – ***P*** wave velocity in the upper layer
- V_{p2} – ***P*** wave velocity in the bottom layer
- V_{s1} – ***S*** wave velocity in the upper layer
- V_{s2} – ***S*** wave velocity in the bottom layer
- ρ_1 – density of the upper layer
- ρ_2 – density of the bottom layer
- α_p – angle of reflection for ***P*** wave
- α_s – angle of reflection for ***S*** wave
- β_p – angle of refraction for ***P*** wave
- β_s – angle of refraction for ***S*** wave

Connections between reflection and transmission coefficients and angles of incident, or offsets, defined by Knott-Zoeppritz equations were extensively analyzed in order to establish usable correlation of seismic characteristics and rock physics. During years many simplified equations of these equations are derived and some of them proved to be

very useful in later developed AVO method. One of the most popular is the Shuey's (Shuey, 1985) approximation of reflection coefficient ***R(α)*** defined as follows

$$R(\alpha) \approx R_0 + \left[A_0 R_0 + \frac{\Delta\sigma}{(1-\sigma)^2} \right] \cdot \sin^2\alpha + \frac{\Delta V_P}{2\,V_P}\left(tg^2\,\alpha - \sin^2\alpha\right) \qquad (31)$$

where are

$\tilde{R}(\alpha)$ – reflection coefficient at the normal incidence
σ – Poisson's ratio
α – angle of incidence
$\Delta V_P = V_{P2} - V_{P1}$
$V_P = (V_{P1} + V_{P2})/2$
$\rho = (\rho_1 + \rho_2)/2$
$\Delta_\rho = \rho_2 - \rho_1$

$$A_0 = B_0 - 2(1 + B_0)\left[\frac{1-2\sigma}{1-\sigma}\right]$$

$$B_0 = (\Delta V_P / V_P)/\left[\frac{\Delta V_P}{V_P} + \frac{\Delta\rho}{\rho}\right]$$

Upper and bottom layer are dented with indexes 1 and 2. Reflection coefficient at normal incidence is defined by the first part of the equation (31), while the second and the third part define reflection coefficients at the incident angle of 30^0 and 60^0. For the angle of incidence less than 30^0, the relation (31) could be approximately rewritten as

$$R(\alpha) \approx R_0 + B\sin^2\alpha \qquad (32)$$

where

$$B = A_0 R_0 + \Delta\sigma/(1-\sigma)^2 \qquad (33)$$

In the relations above ***R_0*** member is known as AVO intercept and the ***B*** member as AVO gradient. Accordingly, the dependence of the reflection coefficient ***R(α)*** on the angle of incidence for P waves is equal to the sum of the reflection coefficient at normal incidence and AVO gradient multiplied with the square of sinus function of the angle of incidence, ***α***. In the relation (33) ***A_0*** is incident amplitude and ***σ*** Poisson's ratio.
Schematic synthetic presentation of seismic wave amplitudes, reflected from the top and the bottom of water and gas saturated sand layer, are shown on ***Fig.11.***

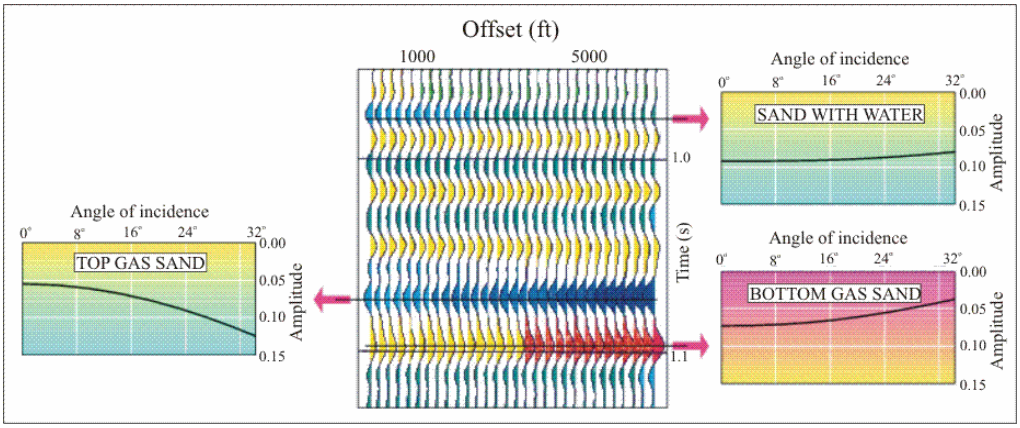

Fig.11: Amplitude change vs. offset and angle of incidence

The amplitude of the seismic wave reflected from the top of gas saturated sand layer, shown on the left side of the figure, increase if the angle of incidence increases. Its polarity became progressively more negative as the offset – dependent on the angle – increases, as shown on the section in the middle part. The reflected arrival from the gas sand bottom, shown at the right lower part of the figure, has the amplitude which became progressively more positive as the angle of incidence increases. Amplitudes reflected from the top of water saturated sand do not change if the angle of incidence or offset changes.

EXAMPLES FROM ADRIATIC SEA

North Adriatic area is located on the eastern foreland ramp of the Apennine Pleistocene foredeep basin as well as on the Dinarid fold and thrust belts, that involves platform (to the East) to basin (to the West) carbonates. Two main tectonic elements are present: the eastern slope of the Dinarid platform, striking NW-SE and NNW-SSE trending antiformal system related to the Dinarid compression phase. In the area several prospects in Pliocene turbidities and Miocene calcarenites associated with biogenic gas were pointed out. Stratigraphic traps in Lower Pliocene channels in the area also exist. The main reservoir rocks are loose shallow sands with porosities between 25 and 35%, filled with biogenic gas.
At the beginning of exploration campaign the main goal of the seismic data interpretation in the area was oriented to establish structural relations and locate the most prospective structural traps. Some discovered bright spot anomalies in the shallow part, like the one presented on ***Fig.12***, located above structural features were not particularly interesting at that time, mainly due to economical consideration (low gas price!).

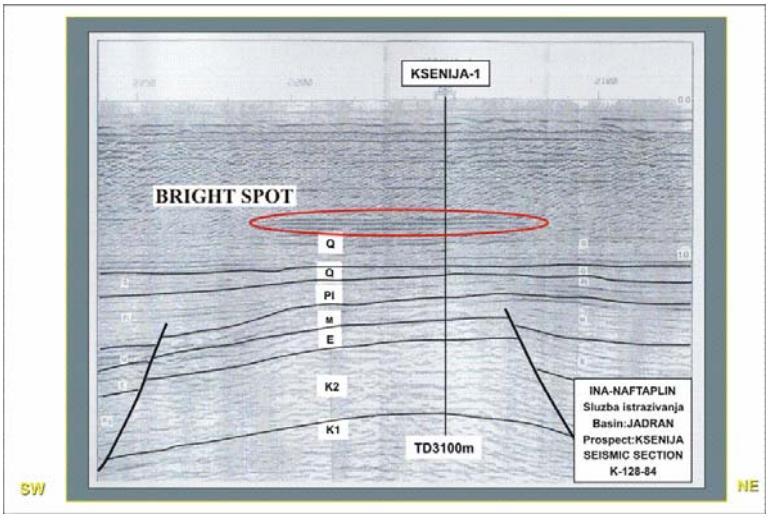

Fig.12: Typical bright spot anomaly in North Adriatic Sea

During structural interpretation it was noticed that some suspicious syncline forms exist on some possible very promising anticline structures. On ***Fig.13*** seismic line passing through such feature with well logs recorded in the well, are presented. At the first glance it seems that the syncline on the seismic section is not interesting at all. However, further analysis and already existing experience in seismic data interpretation in the area confirmed that the noticed push down effect is the cause of the shown false syncline at the top of structural gas trap.

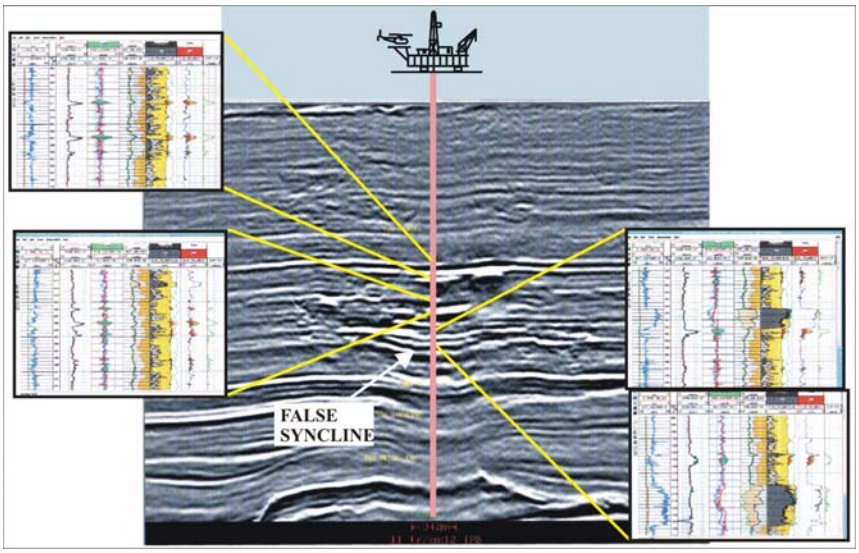

Fig.13: False syncline on 2D seismic section

Seismic time structure map of the surrounding area is shown on ***Fig.14***. Very strong anomalous amplitudes above these false synclines were caused with gas-filled rocks, with very low seismic velocities and the rocks above with normally higher velocities. The final result is the reflection with very strong amplitude and negative polarity ending with diffractions, as presented on the left hand side of the figure, well known as bright spot anomaly. Obviously such features on seismic profile and TWT map were caused by bright spot phenomena and not by poor data acquisition and processing, and definitely not by some locally developed small scale tectonic movements.

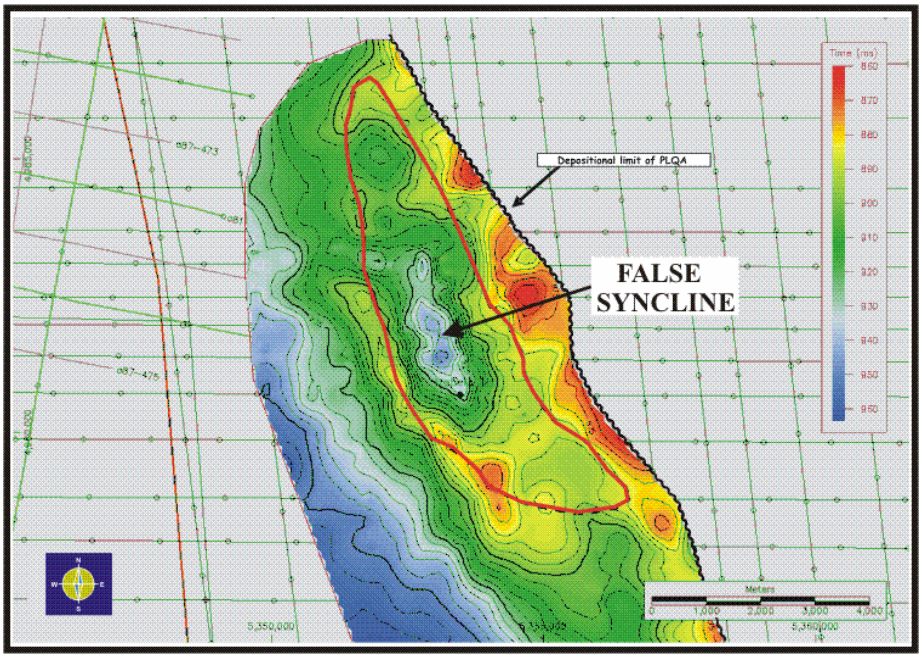

Fig.14: False syncline on seismic two-way-time structure map

On ***Fig.15*** two seismic lines with characteristic bright spot and pull down phenomena are presented. Very pronounced faulting on strong reflection bellow the areas with these effects shows that the bright spot, as well as the push down effects, were formed during

gas leaking through faults. In the marked areas gas accumulations were found above the deeper located faults.

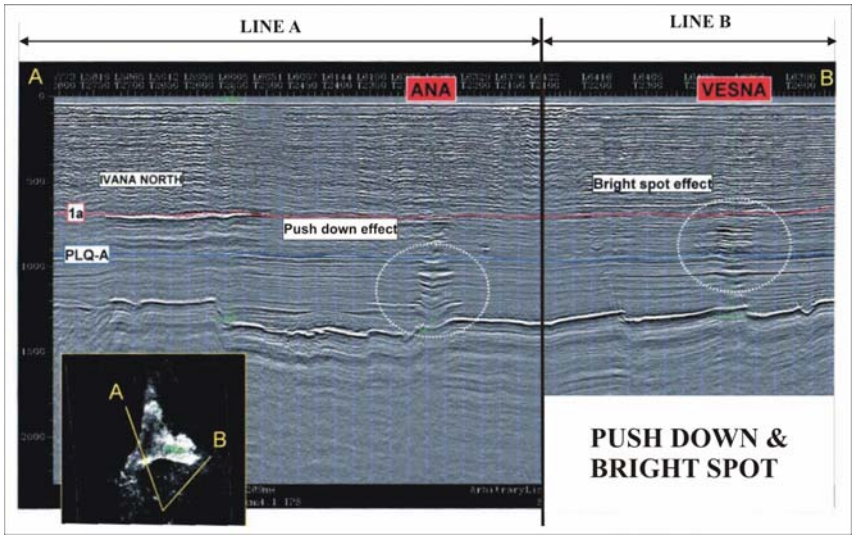

Fig.15: Bright spot and push down phenomena

Recently performed 3D seismic exploration acquisition campaign provided better quality data, enabled more sophisticated approach to bright spot interpretation using special AVO processing and increases the success ratio. The bright spot features with characteristic push down phenomena creating false syncline structure are clearly visible on the seismic section on ***Fig.16***. The located well was a success and proved that the strategy, based on the searching for bright spot effects, should be applied in the future.

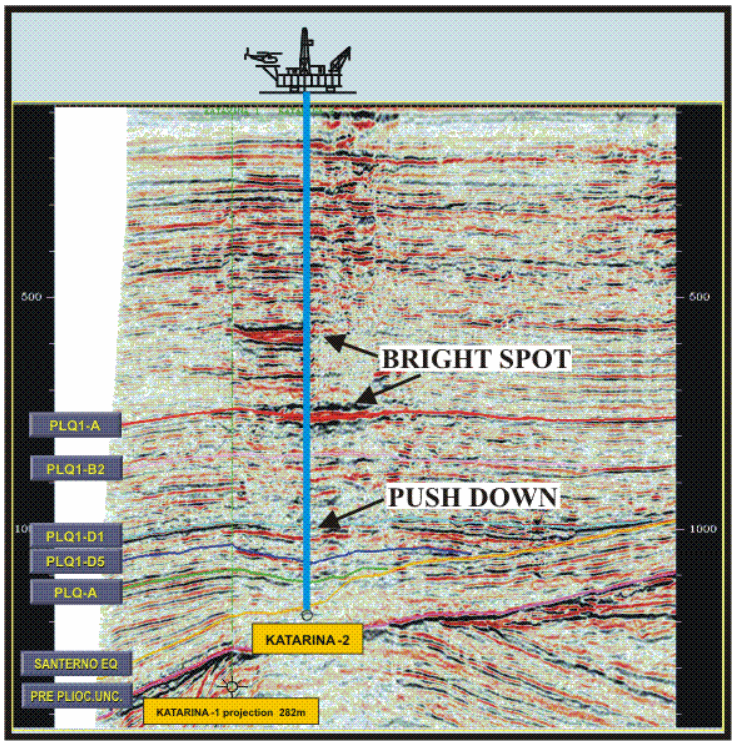

Fig.16: Bright spot effect above gas field

Seismic time structure map with amplitude strength map, shown in the area around the well on ***Fig.16***, is shown on ***Fig.17***. It shows good correlation between seismic time

structure map and amplitude strength and confirm that the “bright spot strategy” is the best exploration strategy for gas field exploration in north Adriatic Sea area.

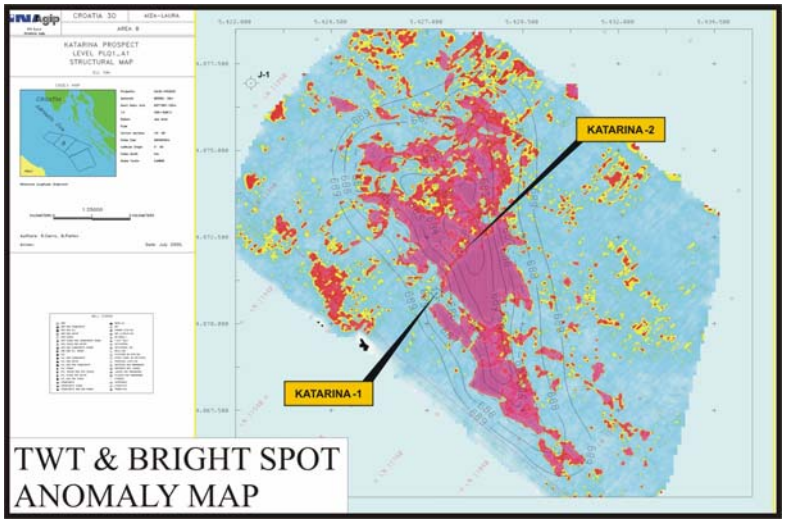

Fig.17: Seismic two-way-time structure map and amplitude strength map

According to the above very limited number of examples it is obvious that the search for bright spot phenomena, based on seismic reflection amplitude analysis, proved to be the most promising method in gas field exploration in North Adriatic area.

CONCLUSIONS

Relations between physical properties of rocks, theoretically established more than a century ago, proved to be very useful in seismic velocity and amplitude determination. Through the analysis of recorded seismic velocities and amplitudes using these relations it is possible to collect useful information concerning rock lithology and fluid saturation. These, however still more qualitative conclusions, proved to be practically very useful.
On the basis of these theoretical conclusions many gas fields were discovered in North Adriatic Sea, some of them already in exploitation. Previous interpretation of seismic data in order to locate possible structural traps was only partially successful. After some gas field discoveries in the area with strong bright spot phenomena, the new exploration strategy based on searching and analyzing such anomalies was successfully applied, resulting in more new producing gas fields.

Acknowledgement

The author would like to thank to the Exploration Department of INA d.d. Naftaplin Co. personnel for providing the material and valuable information necessary in the article preparation.

REFERENCES

1. Allen, J. L., Peddy, C. P., 1993: Amplitude variations with offset: Gulf Coast case studies: SEG Geophysical Development Series, 4

2. Anstey, N. A., 1990: The seismic pulse – Its generation and transmission: GP 202 Exploration Geophysiscs Series, IHRDC

3. Biancone, M., Mariani, M., 2000: Croatia offshore – Aziza Laura Block: Technical evaluation of the exploration potential, ENI AGIP/GEPE-ESPR

4. Bortfeld, R., 1961: Approximation to the reflection and transmission coefficients of plane longitudinal and transverse waves: Geophysics. Prosp., 9, 485-503

5. Castagna, J. P., Batzle, M. L., Kan, T. K., 1993: Rock physics – The link between rock properties and AVO response: u Catagna, J. P., Backus, M. M., eds., Offset-dependent reflectivity – Theory and practice of AVO anomalies, SEG Investigations in Geophysics no. 8, 135-171

6. Churlin, V. V., Sergeyev, L. A., 1963: Application of seismic surveying to recognition of productive part of gas-oil strata: Geolog. Nefti i Gaza, 7, p. 363

7. Forrest, M., 2000: Bright ideas still needed persistence: AAPG Explorer, 21, no. 5, 20-21

8. Gassman, F., 1951: Uber die elastizitat poroser medien: Vierteljahrsschr. Der Naturforsch. Gesellschaft Zurich, 96, 1-21

9. Geldart, L. P., Sheriff, R. E., 2004: Problems in exploration seismology and their solutions, SEG Geophysical References Series No. 14

10. Hilterman, F., 2001: Seismic amplitude interpretation: SEG, EAGE

11. Knott, C. G., 1899: Reflection and refraction of elastic waves with seismological applications: Phil. Mag., 48, 64-97

12. Koefoed, O., 1955: On the effect of Poisson's ratios of rock strata on the reflection coefficients of plane waves: Geophysics. Prosp., 3, 381-387

13. Mavko, G., Mukerji, T., Dvorkin, J., 1998: The rock physics handbook – Tools for seismic analysis in porous media: Cambridge Univ. Press.

14. Ostrander, W. J., 1982: Plane wave reflection coefficients for gas sands at nonnormal angles of incidence: Presented at the 52nd Ann. Internat. Mtg. Soc. Expl. Geophys., Expanded Abstracts, 216-218

15. Ostrander, W. J., 1984: Plane wave reflection coefficients for gas sands at nonnormal angles of incidence: Geophysics, 49, 1637-1648

16. Pan, P. P., de Bremaecker, J. C., 1970: Direct location of oil and gas by the seismic reflection method: Geophys. Prosp., 18, 712-727

17. Rosa, A. L. R., Frasier, C. W., 1976: Extraction of elastic parameters using seismic reflection amplitudes with offset variations: M.S. Thesis, Univ. Of Houston

18. Sengbush, R.L., 1983: Seismic exploration methods, IHDRC, Publishers, Boston, MA 02116, USA

19. Shuey, R. T., 1985: A simplification of the Zoeppritz equations: Geophysics, 50, 609-614

20. Wang, Z., Nur, A. M., 1992: Seismic and acoustic velocities in reservoir rocks – Theoretical and model studies, v. 2, SEG Geophysics Reprint Series, no. 10

21. Zoeppritz, K., 1919: Erdbebebwellen VIIIB, On the reflection and propagation of seismic waves: Gottinger Nachrichten, I, 66-84

Assessment of soil contamination using ToxAlert test

Nóra Kováts[1], Andrea Reichel[1], Tímea Szalay[2], Gábor Bakonyi[3] and Péter Nagy[3]

[1]University of Veszprém, School of Environmental Engineering and Chemical Technology, Veszprém, Hungary. E-Mail: kovats@almos.vein.hu
[2]University of Veszprém, Department of Zoology, Veszprém, Hungary. E-Mail: szalayt@freemail.hu
[3]Szent István University, Department of Zoology and Ecology, Gödöllő, Hungary. E-Mail: bakonyi@fau.gau.hu

Abstract

During the analysis of environmental risk posed by hazardous waste disposal sites numerous questions should be addressed. First of all, whole ecosystems are impacted therefore a complex testing scheme is required where surrogate species represent key elements of the ecosystem. Secondly, considering different exposure routes, direct tests and tests using elutriates should be implied simultaneously. In the first case the organisms are in direct contact with the contaminated soil while in the second case the elutriate might represent the mechanism of runoff or leaching from the soil. The third problem, however, rests in the very complex nature of the medium tested. Soil shows an extremely high spatial heterogeneity, increasing considerably the required number of sampling spots. Our main effort was to test the reliability of a very rapid and cost-effective test, ToxAlert ®100 versus direct tests in the environment of a hazardous waste disposal site and to develop an effective strategy to assess environmental risk posed by hazardous waste of similar composition disposed.

Keywords: soil contamination, superfund, ToxAlert, bioluminescence inhibition, direct tests

1. INTRODUCTION

In the United States detailed methodology is available to assess the environmental risk posed by superfund sites (USEPA, 1997). In Hungary a complex assessment program was initiated in 1996 by the Ministry of Environmental Protection.
Toxicity tests are useful tools in the assessment of superfund sites as they measure the aggregate effect of all the contaminants and furthermore they indicate whether the contaminants are in bioavailable form. However, there are some methodological difficulties implied. First of all, physical variance (texture and chemistry) is an actual property of soils. In order to represent spatial heterogeneity, both vertical and horizontal, sampling spots should be densely located which increases sampling costs.

Another problem is the selection of appropriate endpoints. Assessment endpoints are ecological characteristics which may be adversely affected by the contamination supposed to occur at the site in question (USEPA, 1992). As in the environment of superfund sites whole ecosystems are impacted, ecological risk assessment should evaluate the adverse impact on ecosystem level. Therefore assessment endpoints involve several species which are likely to be exposed to differing degrees and also, they might have different reaction upon the same contaminant. It requires a complex testing scheme where key elements of the ecosystem (mostly trophic levels) are represented by surrogate species (for example Daphnids represent planktonic crustaceans playing an important role in the aquatic food web). Nevertheless, test results do not necessarily correlate with each other in every case.

Also, toxicity tests vary as to the media they analyse. Many standardised tests have been developed for the regulation of aqueous discharges. They do not only use aquatic organisms but the medium is also the elutriate. Toxicity tests using elutriate is useful tool to get information about how different contaminants are transferred from sediment or soil to water. In this way effects of runoff or leaching from soil can be modelled and predicted (USEPA, 1994).

There are tests available which use terrestrial organisms in their original medium. In this case the organisms are in direct contact with the contaminated soil. For example the ISO 11267 standard test is used for assessing the effects of chemicals on the reproductive output of *Folsomia candida* (Collembola).

Such direct tests, however representative they are, have a significant negative aspect: they are time and labour-consuming. Therefore our primary goal was to investigate to what extent a very cost-effective aquatic test, ToxAlert can be used for assessing soil contamination. The survey area was the environment of a hazardous waste disposal site, where contamination caused mainly by heavy metals as well as cyanide and fluoride could be predicted.

The ToxAlert ®100 developed by Merck uses bioluminescence of the bacterium *Vibrio fischeri* as the end-point. Bioluminescence is a natural phenomenon in which visible light is generated by an organism as a result of a chemical reaction. These reactions can be reconstructed outside the organisms from which they originate, thereby enabling exploitation of this natural process. There are diverse types of organisms that display bioluminescence: bacteria, protozoa, fungi, sponges, crustaceans, insects, fish, squid, jellyfish, and lower plants. Bioluminescent organisms occur in a variety of habitats, particularly the deep sea, where light is employed for functions including defence, reproduction and feeding. The enzymes involved in the luminescent (lux) system, including luciferase, as well as the corresponding lux genes, have been most extensively studied from the marine bacteria in the Vibrio and Photobacterium genera and from terrestrial bacteria in the Xenorhabdus genus. It has been found that the light-emitting reactions are quite distinct for different organisms with the only common component being molecular oxygen.

The light output of luminescent microorganisms which emit light as a normal consequence of respiration is read by a luminometer. Chemicals or chemical mixtures, which are toxic to the bacteria, cause changes in some cellular structures or functions such as the electron transport system, cytoplasmic constituents or the cell membrane, resulting in a reduction in light output proportional to the strength of the toxin.

The use of bacteria as test organism has several advantages comparing to conventional toxicity testing. The test is rapid (exposure takes only 30 minutes in contrary to the 24-72 hour period being necessary for other aquatic ecotoxicological tests) and causes no ethical problems. This is a very important issue as in the European Union more and more

effort is made to reduce the number of test animals and to develop alternative test methods (Worth and Balls, 2002). The Chemicals Policy of the EU (European Commission, 2001) explicitly states that among others, the political objective of this policy involves the promotion of non-animal testing.

In order to determine the reliability and accuracy of the test (accuracy in this aspect means to what extent the measured value approaches the real value of a given parameter) results obtained by ToxAlert were compared and correlated to direct ecotoxicological tests and zoological bioindication methods.

Direct tests applied were *Folsomia candida* and *Enchytraeus albidus* reproduction tests.

There are several laboratory test protocols to study pollutant effects on collembolan mortality. One of the first technique was elaborated by Kiss and Bakonyi (1992). A novel handbook (Lokke and van Gestel, 1998) contains soil zoological laboratory test methods, including those for collembolans. Based on the collected knowledge an ISO standard (No. 11267) has been accepted that aims at reproduction studies with *Folsomia candida*.

For enchytraeid worms, or potworms (Oligochaeta: Annelida) there is no generally accepted standard for testing contaminated soils (however, there is an OECD proposal for a new guideline considering *Enchytraeidae* reproduction test). Nevertheless, enchytraeid worms are widely used for toxicological testing in Europe. The generally applied technique studies whether the tested soil inhibits (if yes, to what extent) the multiplication of *Enchytraeus albidus* worms.

Biological indication techniques (including zoological methods) provide information on the extent of toxic and other adverse effects of the tested soils. Terrestrial animals in tests may exhibit contamination effects even when chemical soil pollution levels are below the background values. Thus soil animals can be considered as sensitive biological indicators.

Free-living terrestrial nematodes are important indicators of soil processes, including various disturbances (Samoiloff, 1987; Bongers, 1990; Bongers, 1999; Bongers and Ferris, 1999). Due to several properties (e.g. complexity, high taxonomic variability, a considerable diversity of feeding types and life strategies, different sensitivity to pollutants, etc.) this group is highly suitable for field studies of disturbance effects, including inorganic contamination (heavy metals, microelements), as demonstrated by various authors (Zullini and Peretti, 1986; Weiss and Larink, 1991; Nagy, 1999; Georgieva et al., 2002; Bakonyi et al., 2003; Nagy et al., in press). Therefore the structure of a soil nematode assemblage may serve as an important reference point in soil pollution studies.

2. MATERIALS AND METHODS

30 soil samples were collected in the environment of a hazardous waste disposal site (Fig. 1), from the upper 0.1 m. Each sample consisted of 15-20 composite subsamples serving for the purposes of nematological studies, collembolan and potworm tests as well as ToxAlert probes.

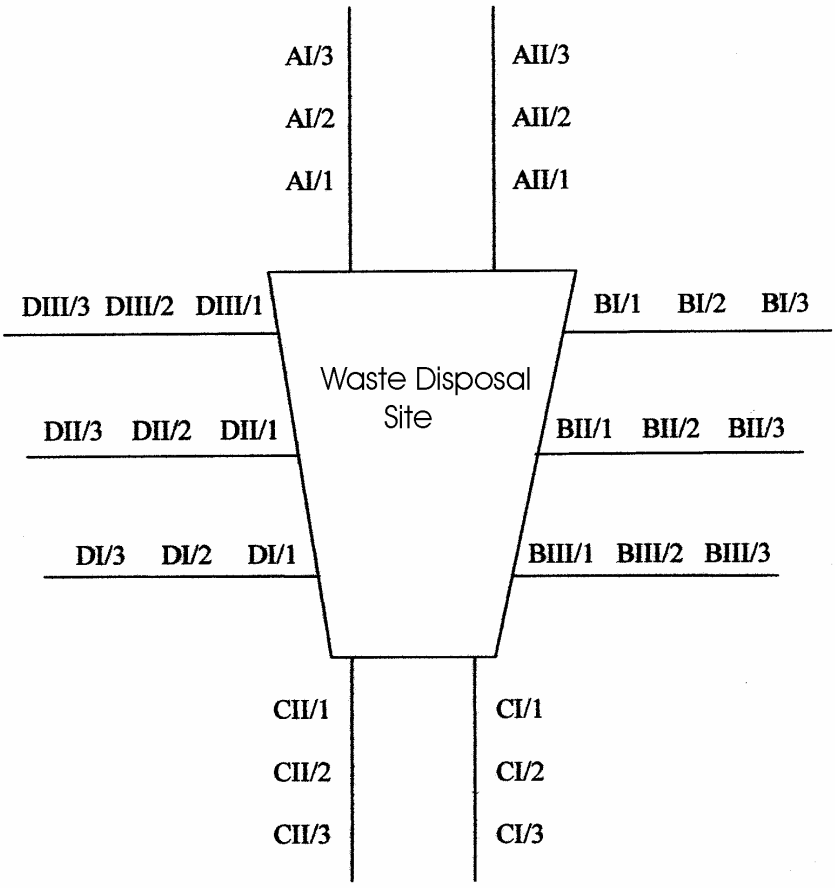

Fig.1. Location of the sampling spots around the waste disposal site.

2.1 ToxAlert test

Elutriate was prepared using 0.1 % dimethyl-sulphoxide (DMSO). In order to provide optimal conditions for the test pH of the samples was adjusted to pH 7.0.
At the beginning of the measurement firstly the test suspension was prepared, using liquid-dried bacteria and reconstitution solution, also provided by Merck. The luminescence intensity of the test suspension was measured in RLU (relative luminescence unit), then the control as well as the sample solutions were added to the test suspension. Luminescence intensity was measured again after the previously set incubation (exposure) time. In our case it was the maximum, 30 minutes.
The ToxAlert ®100 luminometer calculates the inhibition effect (H_t) of the samples automatically in % values. Firstly the f_{kt} correction factor is calculated from the measured luminescence (Equation [1]).

$f_{kt} = I_{kt} / I_0$ (t = 30 min in our test) [1]

where

f_{kt} the correction factor for the contact time
I_{kt} luminescence intensity in the control sample measured in RLU (relative luminescence units), after the contact time
I_0 luminescence intensity of the control test suspension.

Using the correction factor, than the corrected value of for every test sample cuvettes are calculated (Equation [2]).

$I_{ct} = I_0 \times f_{kt}$ [2]

where

f_{kt} mean of f_{kt} of the two control samples

I_0 luminescence intensity of the control test suspension

I_{ct} corrected value of for test sample cuvettes immediately before the addition of the test sample

Then the inhibitory effect H_t of the test sample is calculated (Equation [3]).

$H_t = [(I_{ct} - I_{Tt}/I_{ct})] \times 100$ [3]

where

H_t the inhibitory effect of the test sample after the contact time, in%

I_{ct} corrected value of for test sample cuvettes immediately before the addition of the test sample

I_{Tt} luminescence intensity of the test sample after the contact time, in RLU.

2.2 Collembolan (*Folsomia candida*) test

Folsomia candida is among the most common beneficial springtail species. It has a white colour and no eyes. Adults are 1,5-3,0 mm long. Its furca is long and massive. This species is widely spread throughout Europe in organic soils. Under laboratory conditions it shows parthenogenetic multiplication. It is easy to culture.

In present study the ISO 11267 standard was applied that is meant to test toxicity of contaminants through the reproductivity of *F. candida* under laboratory conditions. During the present experiment two modifications were applied. First, the tests were performed with the exposure of 5, 6 and 7 weeks instead of 4, as demanded by the standard. The reason for this was to obtain a surplus of information, regarding the reproduction rate of the population. Second, the tests were performed on 15 ^{o}C instead of 20 ^{o}C, which also explained the longer duration. The aim of the tests were counting the offspring numbers after the above periods and comparing the collembolan numbers on the different soil samples.

2.3 Potworm (*Enchytraeus albidus*) test

This method provides information on the degree of inhibition of potworm reproduction in the soil samples tested. *Enchytraeus albidus* is a relatively large (max. 15 mm long) member of the annelid group Oligochaeta. It is spread all over the world, especially in organic soils. This species is also widely used and cultured as fish food in aquaria. In our tests adults were used that contained mature eggs. Mature eggs are easy to observe in the clitellum region under a microscope.

Duration of the experiments were 5, 6 and 7 weeks. As an endpoint, potworm numbers were read under a stereomicroscope and adult counts were separated from those of juveniles.

2.4 Nematological analysis

Nematodes were extracted from soil using Cobb's decanting and sieving method (modified according to s'Jacob and van Bezooijen, 1984). Abundance values were estimated under a transmission stereomicroscope (30-40x magnification). After fixing with

80-90 °C hot formalin (cc. 8%) coenological processing meant the identification of at least 150 specimens per sample to genus level.

2.5 Statistical evaluation

In testing environmental media toxicity it provides baseline information to determine whether the sample shows significant toxicity. Toxicity is not significant if the effects do not differ statistically significantly from controls and/or the effects relative to controls are less than 20% (Suter, 1996). According to this, in case of ToxAlert test samples showing bioluminescence inhibition higher than 20% were considered toxic.
For the comparison of animal abundance values, t-tests were applied. Subsequently, exponential curves were fitted to juvenile numbers. Based on this technique population growth rates were read. For curve fitting we used CurveExpert 1.3. (D. Hyams, 112B Crossgate St., Starkville, MS 39759, USA).
Nematode assemblages were studied by the following basic parameters: abundance and taxon numbers. To study significant effects, one-way ANOVA was performed after ln(x+1) transformation of basic data (Statistica for Windows software, Statsoft Inc., Tulsa, USA). As a coenological parameter, Maturity Index (MI) was used (Bongers, 1990).
Correlation amongst different tests was calculated using SPSS for Windows 9.0.

3. RESULTS AND CONCLUSIONS

3.1 Analysis of the soil samples collected in the environment of the waste disposal site

Table 1 gives the results of ToxAlert test for soil samples shown in Fig.1.

Table 1: Results of ToxAlert (Vibrio fischeri) test.

TOXALERT 100		**TOXALERT 100**	
soil sample	inhibition %	soil sample	inhibition %
AI/1	5.8	CI/1	12.65
AI/2	-4.95	CI/2	17.5
AI/3	0.35	CI/3	30.75
AII/1	-2.7	CII/1	0.35
AII/2	-4.55	CII/2	-6.55
AII/3	-7.35	CII/3	36.6
BI/1	-1.1	DI/1	38.65
BI/2	-2.75	DI/2	19.7
BI/3	-1.75	DI/3	-3.0
BII/1	35.1	DII/1	-6.4
BII/2	39.45	DII/2	28.65
BII/3	26.7	DII/3	36.35
BIII/1	-2.7	DIII/1	38.6
BIII/2	26.1	DIII/2	28.95
BIII/3	2.45	DIII/3	29.6

Table 2 gives the results of *Folsomia candida* reproduction tests for soil samples shown in Fig.1.

Table 2: Results of Folsomia candida reproduction test. Numbers refer to juvenile numbers at the end of tests with various treatments. x: unusable samples n: no exponential curve could be fitted

Soil sample	Duration of the test (exposure)			Growth rate (b)	Correlation coefficient (r)
	5 weeks	6 weeks	7 weeks		
AI/1	116	389	493	0.52	0.92
AI/2	139	371	412	0.40	0.88
AI/3	107	416	795	0.80	0.99
AII/1	56	464	907	0.89	0.98
AII/2	77	83	342	1.10	0.97
AII/3	72	394	143	n	-
BI/1	131	311	885	1.0	0.99
BI/2	384	391	832	0.49	0.93
BI/3	181	402	852	0.76	0.99
BII/1	312	493	656	1.01	0.99
BII/2	330	309	720	0.51	0.91
BII/3	228	236	607	0.65	0.95
BIII/1	362	402	883	0.55	0.95
BIII/2	348	411	909	0.58	0.97
BIII/3	363	326	629	0.35	0.86
CI/1	X	97	198	0.61	0.99
CI/2	X	49	474	1.79	0.98
CI/3	X	61	302	1.25	0.97
CII/1	31	345	532	0.61	0.99
CII/2	13	285	548	1.79	0.98
CII/3	156	358	605	1.25	0.97
DI/1	63	103	258	081	0.99
DI/2	48	98	308	1.06	0.99
DI/3	179	168	288	0.14	0.79
DII/1	33	62	108	0.58	0.99
DII/2	22	72	125	0.70	0.78
DII/3	49	63	54	n	-
DIII/1	132	179	324	0.49	0.99
DIII/2	43	92	309	1.13	0.99
DIII/3	52	96	389	1.28	0.99

Table 3 gives the results of Enchytraeus *albidus* reproduction test for soil samples shown in Fig.1.

*Table 3: Results of Enchytraeus albidus reproduction test. Numbers refer to juvenile numbers at the end of tests with various treatments. *: curves were fitted to data, n: no exponential curve could be fitted.*

Soil sample	Duration of the test (exposure)			Growth rate (b)	Correlation coefficient (r)
	5 weeks	6 weeks	7 weeks		
AI/1	0	18	24	12*	0.96
AI/2	0	42	33	16.5*	0.75
AI/3	0	18	34	17*	0.99
AII/1	0	8	54	27*	0.93
AII/2	0	10	39	19.5*	0.96
AII/3	0	3	10	5*	0.97
BI/1	0	27	17	8.5*	0.62
BI/2	5	5	16	0.83	0.95
BI/3	4	52	29	0.31	0.44
BII/1	7	48	10	n	
BII/2	9	11	78	1.68	0.99
BII/3	23	76	53	n	
BIII/1	15	37	59	0.59	0.99
BIII/2	9	23	41	0.67	0.99
BIII/3	5	12	79	1.78	0.99
CI/1	10	12	83	1.67	0.99
CII/2	18	58	102	0.71	0.99
CI/3	27	18	32	0.11	0.38
CII/1	11	10	102	1.88	0.99
CII/2	25	5	162	2.11	0.98
CII/3	23	6	126	1.57	0.96
DI/1	5	6	261	2.46	0.99
DI/2	43	25	189	1.55	0.96
DI/3	29	49	201	1.27	0.99
DII/1	25	13	153	1.84	0.98
DII/2	31	15	158	1.73	0.97
DII/3	33	50	74	0.4	0.99
DIII/1	73	67	57	n	
DIII/2	10	26	210	1.9	0.99
DIII/3	13	65	198	1.18	0.99

Table 4 gives basic data for nematode assemblages in soil samples shown in Fig.1.

Table 4: Basic data for nematode assemblages. MI: Maturity Index, PPI: index for plant feeders. Richness: number of nematode taxa, Abundance: number of nematodes in the sample.

	MI	PPI	Richness	Abundance
AI/1	2.73	2.94	21	2410
AI/2	3.01	2.87	22	1719
AI/3	2.74	X	27	473
AII/1	2.81	2.86	19	976
AII/2	2.39	2.25	19	1163
AII/3	2.93	X	19	1180
BI/1	2.75	2.21	19	1180
BI/2	2.99	X	22	1404
BI/3	2.8	2.68	22	1269
BII/1	2.93	2.63	24	604
BII/2	2.74	2.86	20	1791
BII/3	2.64	X	22	1325
BIII/1	2.65	2.77	20	3059
BIII/2	2.39	2.96	23	918
BIII/3	2.88	2.98	22	1010
CI/1	2.47	X	22	2045
CI/2	2.39	2.47	23	1666
CI/3	2.6	2.31	21	2007
CII/1	2.37	2.13	21	3318
CII/2	2.57	2.71	21	643
CII/3	2.3	2.38	16	3278
DI/1	2.36	2.6	27	2666
DI/2	2.26	X	25	1097
DI/3	2.6	2.65	27	1106
DII/1	2.34	2.33	23	2188
DII/2	X	X	X	2259
DII/3	2.37	2.87	25	1442
DIII/1	2.31	2.24	27	1887
DIII/2	2.59	2.73	24	1193
DIII/3	2.58	2.18	25	1479

3.2 Assessment of soil toxicity

Of soil samples tested the following ones showed bioluminescence inhibition exceeding 20%: BII/1 (35.1%), BII/2 (39.45%), BII/3 (26.7%), BIII/2 (26.1%), CI/3 (30.75%), CII/3 (36.6%), DI/1 (38.65%), DII/2 (28.65%), DII/3 (36.35%), DIII/1 (38.6), DII/2 (28.95%) és DIII/3 (29.65). When plotting them, contaminated areas could be delineated (Fig. 2).
Areas DIII/1 - DII/2 - DIII/3 and BII/1 – BIII/2 – BII/3 are adjacent to the waste disposal site, this fact and their continuity indicate that the disposal site might have really posed an ecological risk. However, toxicity of CI/3 – CII/3 cannot be directly linked to the disposal site and therefore it is difficult to give a clear interpretation. DI/1 shows toxicity while DII/1 does not: it might be caused by either spatial heterogeneity or analytical error.
The maximum inhibition value is 38.65 (DI/1). It indicates that contamination is actually present but the ecological effect on soil fauna cannot be considered as severe.

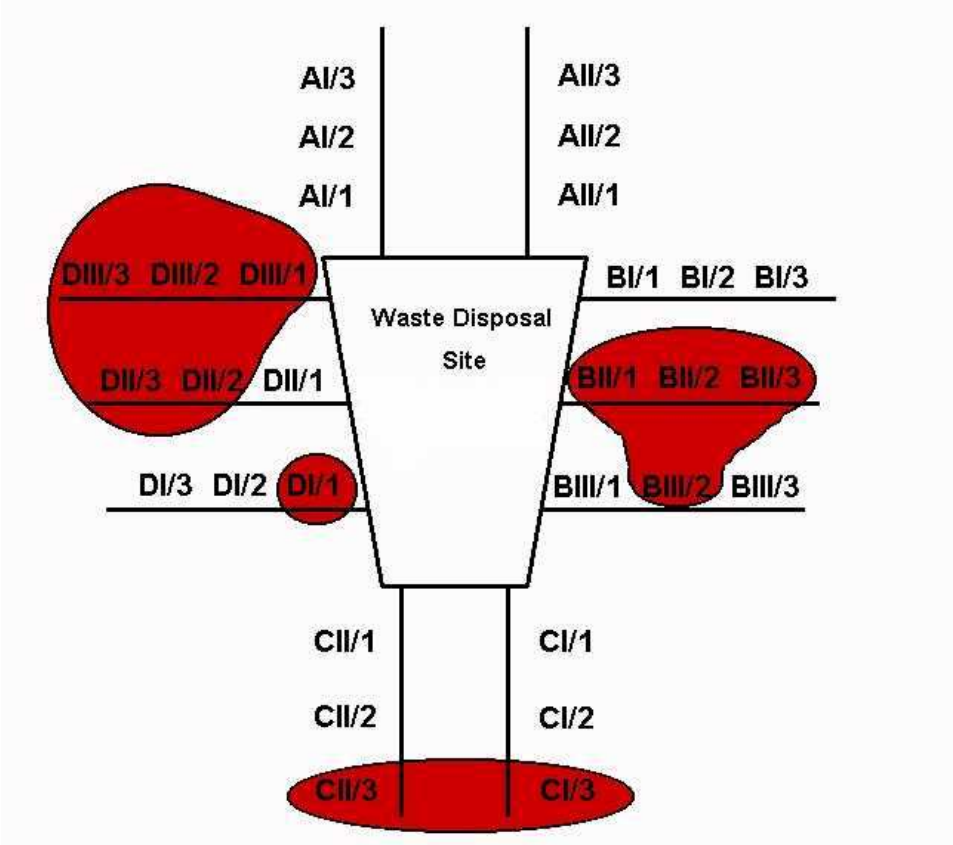

Fig.2. Results of ToxAlert test, red colour indicates samples exceeding 20% bioluminescence inhibition delineating contaminated area.

Based on the *Folsomia candida* test it can be concluded that soil samples taken from the four sides of the hazardous waste disposal site influenced springtail multiplication according to a pattern respective to the localities (Fig. 3).

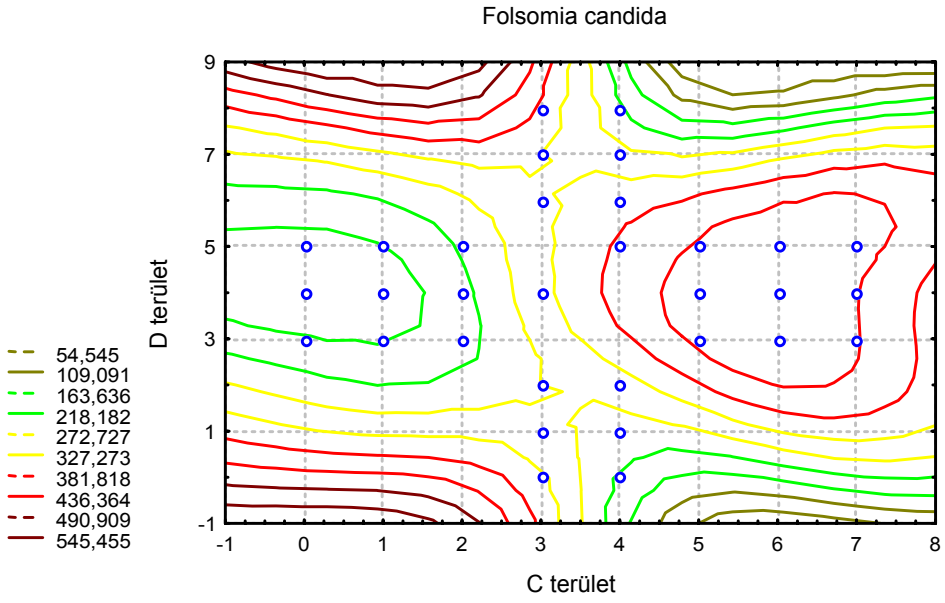

Fig.3. Izoclines derived from *Folsomia candida* offspring numbers.

Most of the collembolans were recorded from the B-side (n=477.5 in average). For the further sides (A, C and D) the average values were 320.9, 258.0 and 137.7, respectively. All these values differed significantly from each other at a minimum level of $p < 0,05$. Population growth rates showed a different pattern. The lowest growth rates could be found in the line of sides B and D also extending over the smelter area, while in samples from sides A and C faster growth could be measured. (Fig. 4).

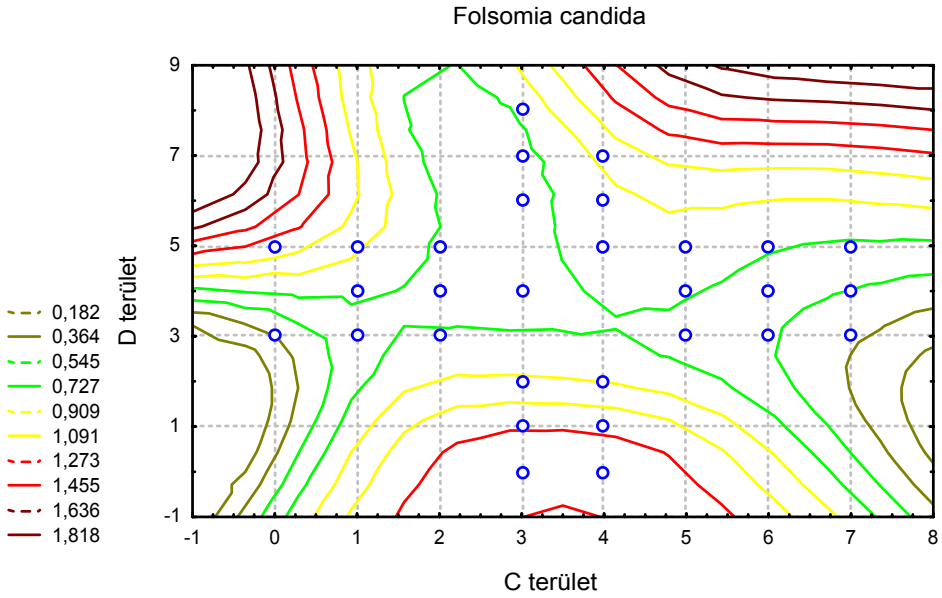

Fig.4. Izoclines derived from *Folsomia candida* growth rates.

Enchytraeus reproductivity tests resulted in the maximum numbers in side D (n=77.0 in average). The following sites were C, B and A with n= 46.1, 27.8 and 16.3, respectively. The differences were significant between sides A and C, A and D as well as B and D, at a minimum level of $p < 0,05$. (Fig. 5).

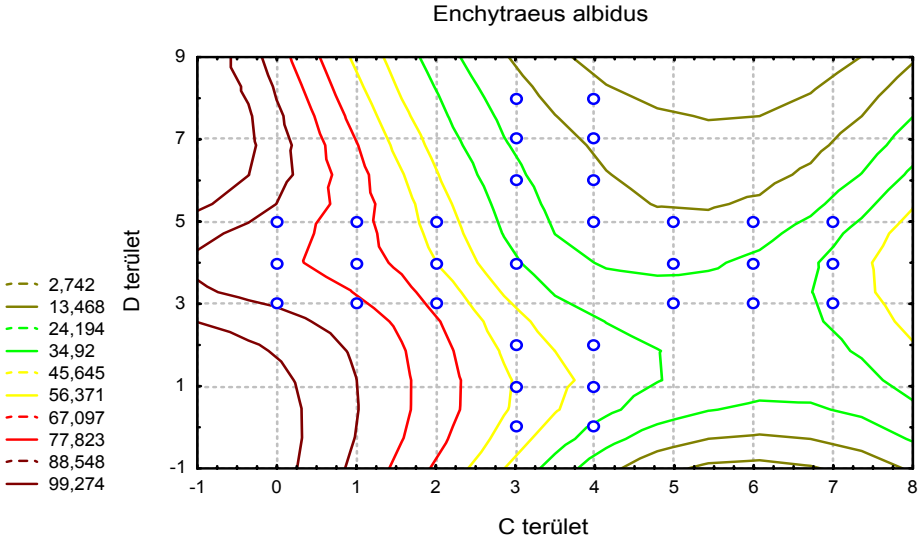

Fig.5. Izoclines derived from *Enchytraeus albidus* offspring numbers.

Population growth rates were the highest in samples from side D, adjacent to the smelter and decreased with the increasing distance (Fig. 6).

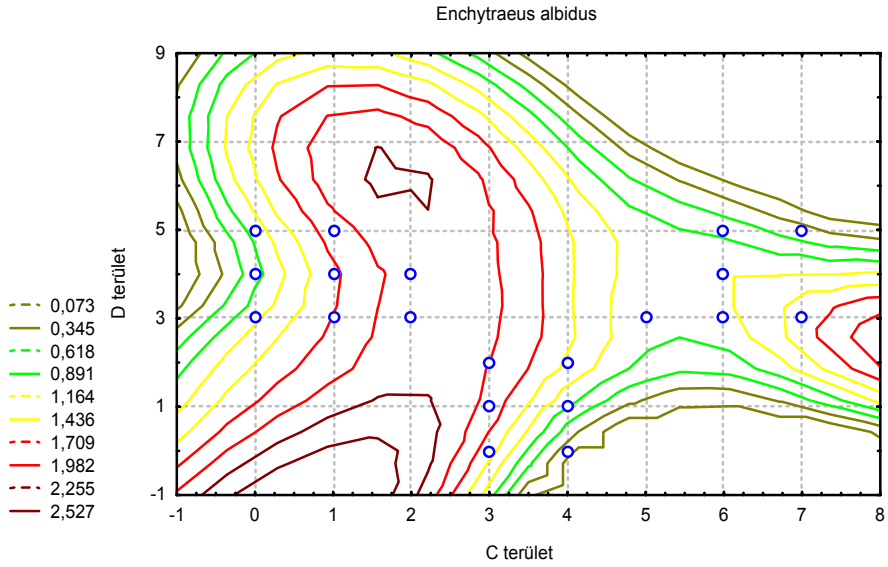

Fig.6. Izoclines derived from *Enchytraeus albidus* growth rates.

It has to be pointed out that in the laboratory tests it was not possible to apply an absolute control. The soil type-related effects being often higher than treatment effects it was not reasonable to involve such a control (e.g. OECD soil).
Nematode abundance values give no sign of possible distance-dependent effects. Neither could be determined any systematic side-dependent effect. Only data from side C were higher than those from other samples. The abundance values for the zone closest to the smelter are in average slightly higher than the others. However, this difference is not significant. Taxon numbers show no distance dependence either, but there appears a significant difference ($p < 0,01$) with the highest values in samples from side D.
In terms of Maturity Indices there is a pair-wise difference: values in samples from sides A and B are higher than those in C and D. The difference over 10% measured in this study can be termed considerable in case of such a derived index. This is supported by the statistically significant difference ($p < 0,05$) among the various side areas. Along the distance gradient an insignificant increase of the MI was detected.
Regarding PPI, samples from all but C side show high values (PPI=2.8 and over). However, occurrence of these values is absolutely sporadic. Moreover, in PPI values the nutrient supply capacity of the plant cover plays an important role besides the pollution. Therefore results of this parameter could not be evaluated consistently in this study.
Both nematode abundance and taxon richness values correspond to data measured in comparable agroecosystems. Thus these parameters give no alert of any possible disturbance. MI values in sides A and B are definitely high, while in the two other localities are within the range observed in comparable agricultural fields in Hungary (Bakonyi et al., 2003, Nagy et al., in press.).
We might come to the final conclusion that by ToxAlert contaminated areas could be delineated to some extent, while zoological parameters are not sensitive enough to

measure minor differences between soil samples with low or negligible of pollution. This is indicated by the fact that parameters measured in *Folsomia candida* and *Enchytraeus albidus* laboratory reproductivity tests as well as nematological indices show no clear distance-dependent effects, i.e. the growth of reproduction rate with the increasing distance from the source of contamination.
Even though contaminated areas delineated by ToxAlert cannot be clearly seen from other numerical test results, a certain correlation was found between ToxAlert and *Enchytraeus albidus* reproduction as well as between ToxAlert and the Maturity Index (Table 5). The correlation is negative, as increase in bioluminescence inhibition correlates with the decrease in *Enchytraeus albidus* reproduction and in Maturity Index, all meaning a certain degree of toxic contamination in the respective samples.

Table 5: Correlation amongst ToxAlert, Folsomia candida and Enchytraeus albidus reproduction as well as certain nematological parameters. FC reprod.: Folsomia candida reproduction, EA reprod.: Enchytraeus albidus reproduction, MI: Maturity Index, PPI: index for plant feeders (Plant Parasite Index), Taxon: number of nematode taxa, Abund.: Nematode abundance in the samples. Bold figures refer to a significant correlation at the 0.01 level (2-tailed).

		Tox Alert	**FC reprod.**	**EA reprod.**	**MI**	**PPI**	**Taxon**	**Abund.**
Tox Alert	Pearson Correlation	1.000	0.292	**-0.416**	**-0.392**	-0.048	0.283	0.180
	Sign (two-tailed)		0.131	0.031	0.036	0.826	0.137	0.341
	N	30	28	27	29	23	29	30
FC reprod.	Pearson Correlation	0.292	1.000	-0.075	-0.222	0.008	0.328	0.251
	Sign (two-tailed)	0.131		0.722	0.265	0.972	0.095	0.198
	N	28	28	25	27	22	27	28
EA reprod.	Pearson Correlation	**-0.416**	-0.075	1.000	0.323	0.106	-0.210	-0.283
	Sign (two-tailed)	0.031	0.722		0.107	0.649	0.304	0.152
	N	27	25	27	26	21	26	27
MI	Pearson Correlation	**-0.392**	-0.222	0.323	1.000	**0.475**	-0.206	**-0.383**
	Sign (two-tailed)	0.036	0.265	0.107		0.022	0.283	0.040
	N	29	27	26	29	23	29	29
PPI	Pearson Correlation	-0.048	0.008	0.106	**0.475**	1.000	0.030	-0.298
	Sign (two-tailed)	0.826	0.972	0.649	0.022		0.892	0.167
	N	23	22	21	23	23	23	23
Taxon	Pearson Correlation	0.283	0.328	-0.210	-0.206	0.030	1.000	-0.271
	Sign (two-tailed)	0.137	0.095	0.304	0.283	0.892		0.156
	N	29	27	26	29	23	29	29
Abund.	Pearson Correlation	0.180	0.251	-0.283	**-0.383**	-0.298	-0.271	1.000
	Sign (two-tailed)	0.341	0.198	0.152	0.040	0.167	0.156	
	N	30	28	27	29	23	29	30

ToxAlert proved to be effective in assessing risk posed by this hazardous waste disposal site. *Vibrio fischeri* test has widely been successfully applied to detect soil and sediment contamination (e.g. Bennett and Cubbage, 1992; Svenson et al., 1996; Johnson and Long, 1998). Doherty (2001) concludes that for many chemicals tested, the results obtained through in laboratory testing with the *Vibrio fischeri* test are often consistent with the results of other ecotoxicological tests and with analytically derived concentration of the contaminant. However, Bennett and Cubbage (1992) recommend the test to be used separately to screen many samples and for inclusion in a multispecies test where risk is evaluated based on the results of several different bioassays.
This test is not only reliable but very rapid: preparation of the elutriate takes app. 45 minutes, performing the test takes another 45 minutes (in case the maximum exposure,

30 minutes is selected, but for screening-level tests even 5 minutes exposure can be enough).
Another advantage of the test is its precision. Precision – defined as measurement of variability in the data collection process (USEPA 1997) – is one of the key components of quality assurance in risk assessment. In case of ecotoxicological tests variability among parallel measurements is meant. The main cause of variability is that individuals normally show different sensitivity to the same toxicant. It follows a predictable statistical distribution with most organisms having approximately the same (average) sensitivity and few being more sensitive or less sensitive. The frequency distribution of sensitivity is assumed to follow a log-normal distribution. However, in case of ToxAlert the number of test organisms is of order of million therefore this source of error can be minimised.
Considering the accuracy, reliability and easy-to-perform nature of the test, it can be recommended to be used in the diagnostic phase of superfund management, significantly reducing the costs.

ACKNOWLEDGEMENTS

This research was funded by the National Research and Development Programme.

REFERENCES

Bakonyi G., P. Nagy and I. Kádár (2003): Long term effects of heavy metals and microelements on nematode assemblage. Toxicology Letters 140-141: 391-401.

Bennett, J. and J. Cubbage (1992): Review and Evaluation of Microtox® Test for Freshwater Sediments. Environmental Assessment Program Report, 92-e04

Bongers A.M.T. (1990): The maturity index: an ecological measure of environmental disturbance based on nematode species composition. Oecologia 83: 14-19.

Bongers A.M.T. (1999): The Maturity Index, the evolution of nematode life history traits, adaptive radiation and c-p scaling. Plant and Soil 212: 13-22.

Bongers A.M.T. and Ferris H. (1999): Nematode community structure as a bioindicator in environmental monitoring, Trends Ecol. Evol. 14: 224-228.

Commission of the European Communities (2001). White Paper. Brussels

Doherty, F. G. (2001): A Review Of The Microtox® Toxicity Test System for Assessing the Toxicity of Sediments and Soils. Water Quality Research Journal of Canada, 36(3): 475-518

Georgieva S.S., S.P. McGrath, D.J. Hooper and B.S. Chambers (2002): Nematode communities under stress: the long-term effects of heavy metals in soil treated with sewage sludge. Applied Soil Ecology 20: 27-42.

Johnson, B.T. and E.R. Long (1998): Rapid toxicity assessment of sediments from estuarine ecosystems: A new tandem in vitro testing approach. Environ. Toxicol. Chem. **17**(6): 1099-1106

Kiss I. and G. Bakonyi (1992): Guideline for testing the effects of pesticides on Folsomia candida Willem (Collembola): laboratory tests. in Hassan S. A. (ed.): Guidelines for Testing the Effects of Pesticides on Beneficial Organisms: Description of Test Methods. IOBC/WPRS Bulletin XV:131-138.

Lokke H. and C.A.M. Van Gestel (1998): Handbook of soil invertebrate toxicity tests. John Wiley & Sohn.Chichester, England.

Nagy P. (1999): Effects of an artificial metal pollution on nematode assemblage of a calcareous loamy chernozem soil. Plant and Soil 212: 35-47.

Nagy P., G. Bakonyi, T. Bongers, I. Kádár, M. Fábián and I. Kiss: Effects of microelements on soil nematode assemblages seven years after contaminating an agricultural field. The Science of the Total Environment, in press.

Samoiloff, M.R. (1987): Nematodes as indicators of toxic environmental contaminants. In: J.A. Veech, D.W. Dickson (eds.), Vistas on Nematology, E. O. Painter Printer Co., DeLeon Springs, Florida, pp. 433-439.

s'Jacob J.J. and J. van Bezooijen (1984): A manual for practical work in nematology, Wageningen Agricultural University Department of Nematology, 77 pp.

Suter, G.W. (1996): Risk Characterization for Ecological Risk Assessmnent of Contaminated Sites. Prepared by the Environmental Restoration Risk Assessment Program, Lockheed Martin Energy Systems, Inc., Oak Ridge, Tennessee, ES/ER/TM-200

U.S. Environmental Protection Agency (1992): Framework for Ecological Risk Assessment. EPA/630/R-92/001. Risk Assessment Forum, Washington, DC.

U.S. Environmental Protection Agency (1994): Using Toxicity Tests in Ecological Risk Assessment. Eco Update Intermittent Bulletin Vol. 2. No. 1. Office of Solid Waste and Emergency Response.

U.S. Environmental Protection Agency (1997): Ecological Risk Assessment Guidance for Superfund: Process for Designing and Conducting Ecological Risk Assessments. EPA 540-R-97-006.

Weiss, B. and O. Larink (1991): Influence of sewadge sludge and heavy metals on nematodes in an arable soil. Biol. Fertil. Soils 12: 5-9.

Worth, A. and M. Balls (2002): Alternative (non-animal) methods for chemical testing: current status and future prospects. A report prepared by ECVAM and the ECVAM Working Group on Chemicals. European Centre for the Validation of Alternative Methods, Institute for Health & Consumer Protection, European Commission Joint Research Centre, Ispra

Zullini A. and E. Peretti (1986): Lead pollution and moss-inhabiting nematodes of an industrial area. Water, Air, Soil Pollut. 27: 403-410.

JOURNAL OF HUNGARIAN GEOMATHEMATICS

Volume 2

Determination of drainage network in digital elevation models, utilities and limitations

Richárd Kiss[1]

[1]University of Szeged, Department of Physical Geography and Geoinformatics (ricsi@earth.geo.u-szeged.hu)

Abstract

The starting point for the examination of different catchments is the determination of drainage network. This network forms the basis of many further examinations, such as the determination of subcatchments, river networks, and morphometric examinations. If there is a greater catchment area, there is a demand for a more detailed presentation and examination of the network than the automatically derived digital elevation model of the area or the hydrograph of topographic maps.
The importance of the task is shown by the fact that methods supported by the computer technology appeared as early as the beginning of relief analysis. Dozens of different algorithms have become well-known during the last fifteen years.
This presentation outlines the most important methods of the automated mapping of flow routing, highlighting their utilities and limitations. Then a complex procedure, which combines the favourable characteristics of different methods, will be presented.
The results will be demonstrated on the example of a particular catchment.

Keywords: model, hydrology, geomorphology, runoff, channel, catchment.

1. INTRODUCTION

One of the recent central topics of environmental agenda is the presence of water in our environment. Studying the causes of floods, pollution of rivers and developing prevention methods directed attention to the examination of catchment areas.
Topography plays an important role in the movement of waters flowing on the surface. Water flows downwards on the surface, towards the steepest slope. The result of defining flow direction for each point of the catchment area is the flow network of the catchment. Analysing this network we can distinguish different types of downflow. On the upper parts of catchments there are primarily surfaces and subsurfaces, with non-linear runoffs. Linear channel flows are formed by narrow channels as these waters gather on the convergent surface.
There are various methods to determine the drainage network of a given area. Based on a detailed topographic map, we can define the drainage lines from the hydrographical elements.

However, the result that we obtain is not detailed enough for large-scale examinations. The ground survey of a study area is time-consuming and expensive; furthermore the quality of the result is often not homogeneous spatially.

Nowadays, it is becoming more and more common to determine drainage networks from digital elevation models.
The first attempts at determining drainage networks (Peucker and Douglas, 1975) did not result in actual runoff, but it was also true that the capacity of computers in those days would not have been sufficient enough to allow the application of more complicated models. Several new algorithms have been presented by different authors since then. Most of these are based on cell-based grid model (Fairfield and Leymarie, 1991; Costa-Cabral and Burgess, 1994; Freeman, 1991; Lea, 1992; Tarboton, 1997), but there have also been applications of TIN (Jones et al., 1990; Nelson et al., 1994) and contour-line models, too (Moor, 1991).
Generally, these algorithms have not become widespread because of their complexity or did not provide appropriate results. Today the most commonly used method is Deterministic 8 (O'Callaghan & Mark, 1984), while other methods are mainly applied in research projects.

In this paper I will outline three different methods and their combinations for the extraction of channel networks from digital elevation models. These are the following:

- hydrological approach — flow accumulation
- morphological approach — convergence
- morphological process approach

2. METHODS

One of the most commonly used digital data model of the Earth's diverse surface is a digital elevation model (DEM), which describes the surface with elevation defined at intersection points of grid-lines. These elevation values are stored in a cell-based grid model (Fig.1, Fig. 2)
Most of the hydrological models require a so-called hydrologically correct DEM, which means that starting out from any cell and following the greatest slope we can reach the edge of the DEM, consequently the DEM does not include sinks. Several methods are known for creating hydrologically correct DEM e.g. filling sinks or deepening drainage routes (Hutchinson, 1989).
If the DEM contains flat areas (mostly produced by the method of filling sinks), we can't use the simple aspect based flow models. In this case we have to add some other algorithms to the flow model to handle the flat area problem. In this paper we use the method of filling sinks, which produced no flat areas (Planchon and Darboux 2002).

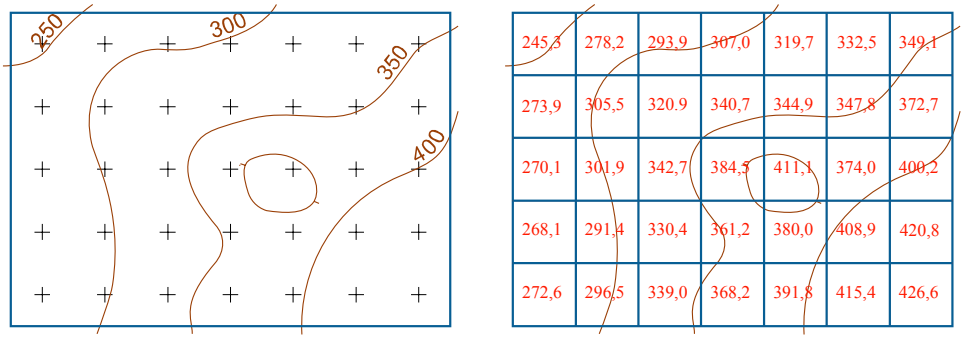

Fig. 1. Cell based digital elevation model (DEM)

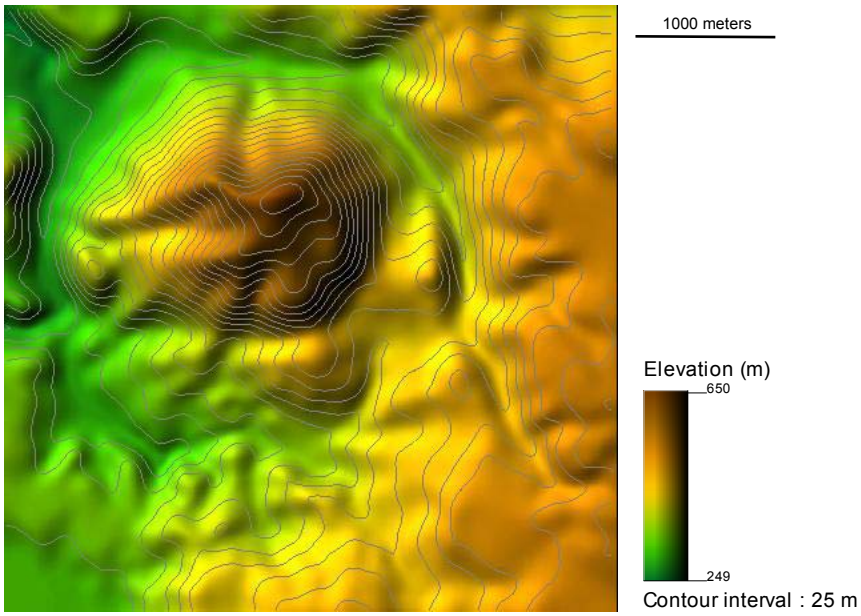

Fig. 2. Digital elevation model of the Karancs-Medves area

2.1. Hydrological approach — flow accumulation

The common characteristic of flow accumulation models is that they all determine the catchment area regarding each cell of the DEM. Those cells whose catchment areas exceed a certain size can be marked as linear flows. The difference between all the models lies in the way they determine flow direction.

Deterministic 8 (D8) model (O'Callaghan and Mark, 1984)

In this model, in the case of each cell-water can flow to the area of any adjacent cell towards the steepest slope. This model results in eight possible flow directions, which is referred to in the name of the model (Fig. 3). We determine the steepest descent slope from a cell to its steepest downslope neighbour with a simple formula taking the elevation of the adjacent cells and the distance between the centres of cells into consideration.

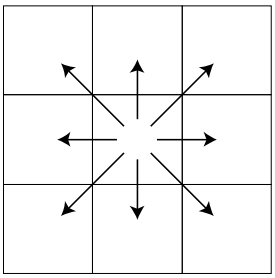

Fig. 3. The eight possible flow direction

This model is simple and traditional, therefore it is the most commonly used cell-based runoff model. General Geographical Information Systems (GIS) using cell-based models apply this model almost exclusively.
If we examine the flow accumulation result of the model, we can clearly see the main lines of the drainage network (Fig. 4). However, in the case of divergent or planar areas, where non-linear flow conditions (surface and subsurface runoffs) are prevalent, the model is not realistic. A lot of cells seem to be without inflow, although they are not situated on a drainage divide. The reason for this lies in the delimitation of flow directions to eight. On planar slopes where aspect is between two possible directions, eight directions prove to be too few. In this case we get parallel orthogonal or diagonal drainage lines, because flow direction cannot exactly match the aspect.

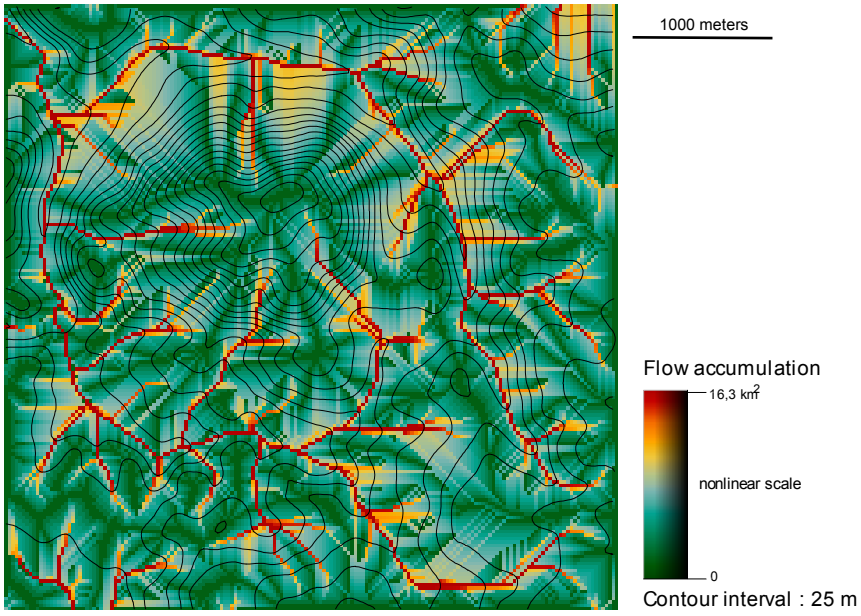

Fig. 4. The flow accumulation result of the D8 model

To obtain a channel network from the D8 model, we must define a threshold value serving as a minimum value when selecting cells with catchment areas for channels.
By analysing three different threshold values we can see that if the value we choose is too small, errors can be detected even along those channels that are correctly determined. These errors can be eliminated by increasing the threshold value, but after this modification the number of determined channels will be decreased (Fig. 5). There is no general rule to

establish threshold values. Among other things the optimal scale of thresholds may depend on the scale of the model or the morphological and geological characteristics (e.g.: drainage density, relief energy) of the area.
By edging away from the drainage divide the value of flow accumulation increases exponentially, makes establishing a correct threshold value even more problematic.

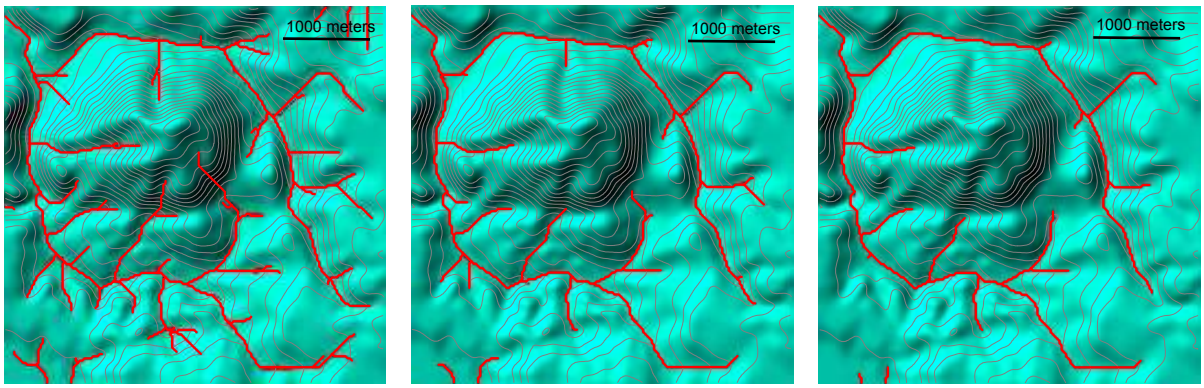

Fig. 5. The channel network from the D8 model. The threshold values are 50000 m^2, 150000 m^2 and 250000 m^2

Multiple flow direction (MFD) model (Freeman, 1991)

This model considers drainage of a divergent flow, so the drainage of the particular cells flows downslope to several adjacent cells of lower elevation. The scale of divergence is determined by the slope of the cell. Similarly to the D8 model, the calculation of flow accumulation to each adjacent cells (i=1..8) is simple and is done by the following formula:

$$f_i = \frac{\max\left(0, S_i^p\right)}{\sum_{j=1}^{8} \max\left(0, S_j^p\right)}$$

where S_i, S_j is the slope to adjacent cells (if $cell_i$ is upwards, then $S_i < 0$; if $cell_i$ is downwards, then $S_i > 0$; if the two adjacent cells have the same height, then $S_i = 0$), P is the weighting of divergence, based on the analyses the optimal value can be determined as 1.1.
Examining the result (Fig. 6) we can see that the MFD model's result is only realistic in divergent surface and subsurface drainage circumstances, while along linear flows — especially at wide valley bottoms — the resulting divergence is not realistic. The effect is rather like a wet zone than a narrow channel. Therefore, the model cannot be applied for the threshold-based direct channel determination specified under the D8 model, since the resulting network is often unconnected.

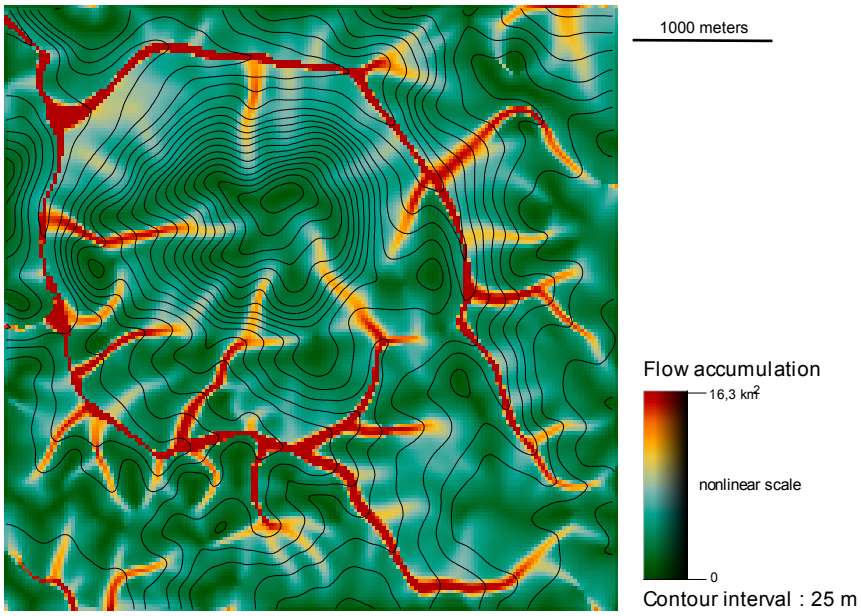

Fig. 6. The flow accumulation result of the MFD model

MFD-D8 model

Analysing the previous two models we can see that they complement each other: the divergent MFD model can be applied at the initial, upper parts of flows, while the D8 model has good results for linear flows. For the switching between the models another threshold value can be applied. The result of such a hybrid model is demonstrated on Fig. 7.

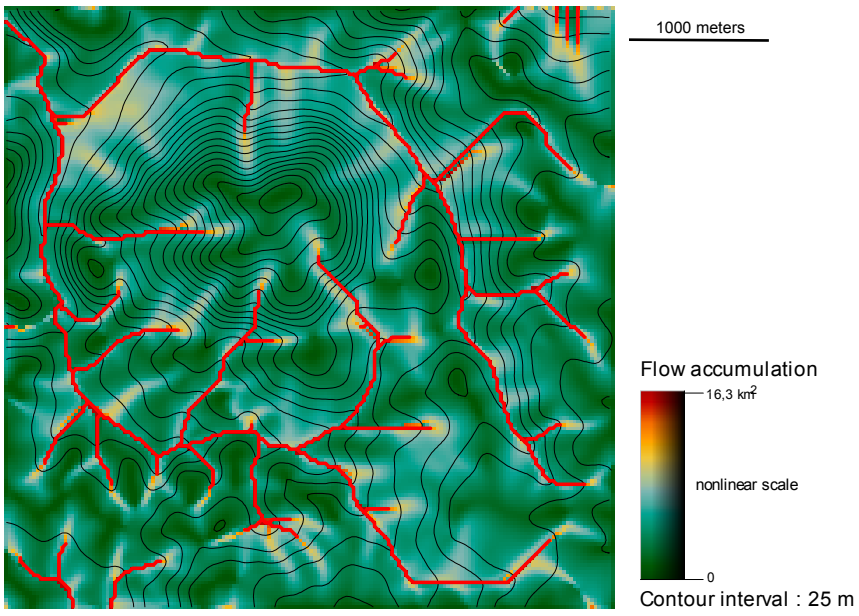

Fig. 7. The flow accumulation result of the MFD – D8 model

Assessing flow accumulation methods we can conclude that the critical point of the models is determining the threshold value for linearity.

2.2. Morphological approach: Convergence index

Several types of convergence index are known. In the following we will examine the simplest of them, which determines convergence index on the basis of aspect (Köthe and Lehmeyer, 1994) . The index is obtained by averaging the bias of the slope directions of the adjacent cells from the direction of the central cell, and substracting 90 degrees. The possible values of the index range from –90° to +90° according to Fig. 8.

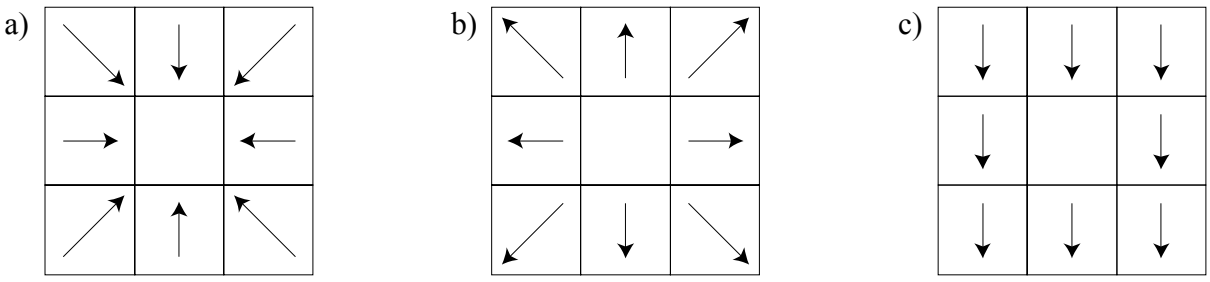

Fig. 8. Calculating the convergence index on the basis of aspect. The averages of the relative aspects are 0° (a), 180° (b), and 90° (c). The convergence indexes are -90° (a), 90° (b), 0° (c)

Figure 9 demonstrates the spatial distribution of the convergence indices on the study area. The result shows the morphological structure of the area clearly, ridges and valleys are well-defined. However, just as in the case of the MFD method, this approach is unsuitable for obtaining a drainage network.

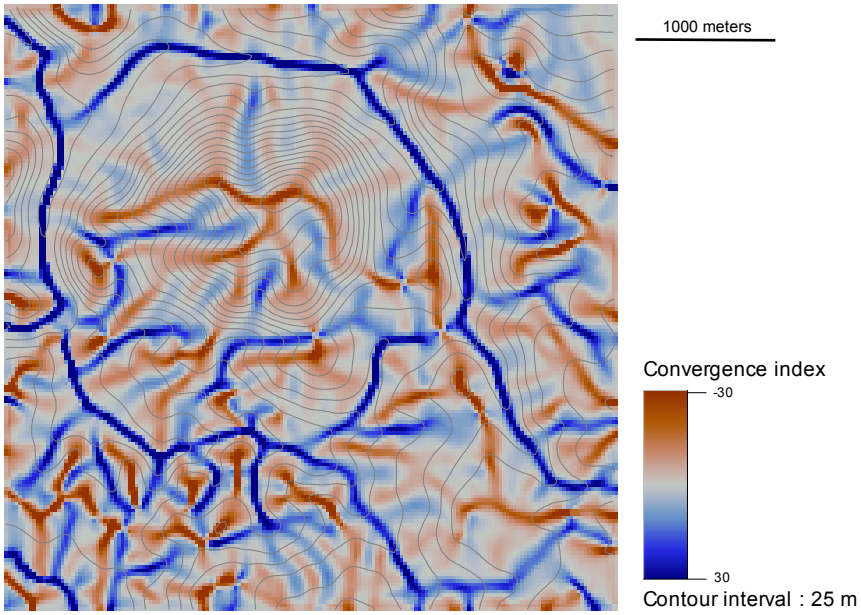

Fig. 9. The spatial distribution of the convergence index

MFD-D8-convergence threshold model

As we can see, on the basis of the convergence index we can draw conclusions concerning the nature — convergent or divergent — of the flow, and thus concerning the linearity of the flow. Therefore it can be used as a spatial threshold-value of the MFD-D8 model. The model is

structured as the following: according to the MFD model, we calculate flow accumulation values beginning from drainage divide to that point where the convergence-index is smaller than a certain threshold-value defined before. From this point we apply the D8 model. To reduce errors, as a further basic condition to linearity, we can establish the minimum length, under which the convergence value must remain under the threshold-value.
In this case we also establish the threshold-value by trial and error.
Looking at the result of the model we can see that channels are more clearly defined than in the previous models (Fig. 10). As opposed to flow accumulation models, the advantage is that we also obtain the actual channels for those catchment areas which are not fully covered by the given dataset (we can find such catchment areas at the edge of the DEM). In the case of flow accumulation models, catchment size can be calculated from the edge of the DEM, this way the calculated catchment size will be smaller than in reality.

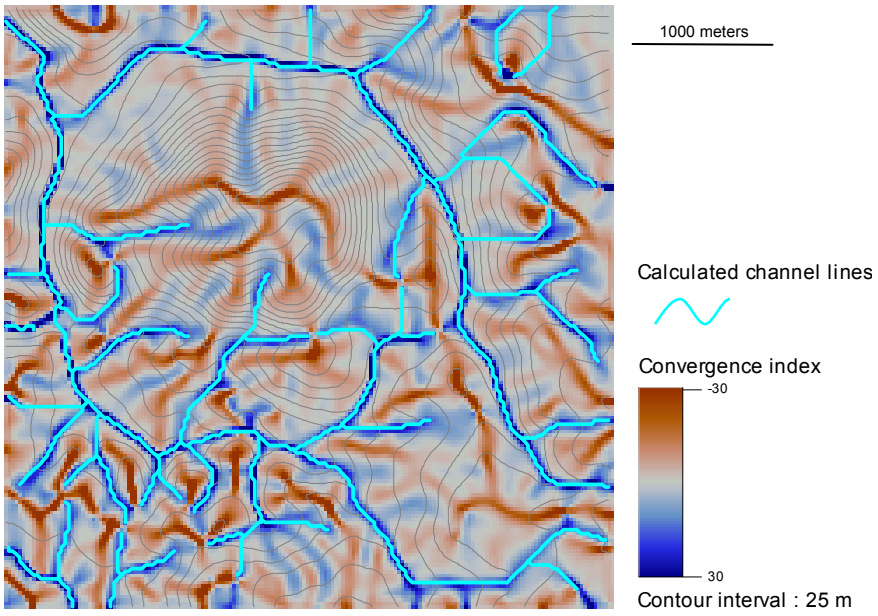

Fig. 10. The channel network determined with convergence-threshold model

2.3. Geomorphological-process competition for channel initiation

This model is based on different landscape evolution models.
The relief of the Earth was formed by the competition of different processes between hillslope and channel processes (Kirkby, 1986, 1993; Willgose et al., 1991; Howard, 1994, Tucker and Brass, 1998).

For the modelling of hillslope processes (freeze-thaw, rainsplash, bioturbation, etc) the diffusive hillslope transport model is used. According to this model the intensity of hillslope processes (H) is proportional to the degree of slope.

$$H = k_d S$$

where S is slope and k_d is a constant.

For channel processes we must differentiate between two cases: 1. if the surface is covered by easily abrading regolith, the amount of sediment flux is maximised by sediment transport capacity (transport limited model); 2. if the surface is more resistant (bedrock, dense vegetation), the scale of erosion can remain under the transportable amount of materials (detachment-limited case), and it depends on how fast the transportable materials form.
Here we model the transport limited case. According to this model, the amount of transportable material by the linear runoffs depends on the amount of water running off the surface, and the degree of slope. The following formula is used to calculate the water-borne sediment flux, Q_s (Tucker and Brass, 1998):

$$Q_s = k_f Q^m S^n$$

where Q is the total surface water discharge, S is slope and k_f, m, n are constants.

$$Q_s = k_f (PA)^m S^n$$

where A is the contributing area, P is a constant and $Q = PA$.
For a hillslope profile, the point of transition from diffusion-dominated to runoff-dominated erosion can be defined as the point at which the two processes are equally effective in transporting sediment (Howard, 1997):

$$k_d S = k_f (PA)^m S^n$$

$$\frac{k_d}{k_f P^m} = A^m S^{n-1}$$

If $\theta_l = \frac{k_d}{k_f P^m}$ and $l = n - 1$, this reduces to

$$\theta_l = A^m S^l$$

So the result is that there is transition between the processes, where $A^m S^l$ reaches θ_l value, which can be interpreted as a threshold-value for linearity.
From the model discussed above we can draw that useful conclusion that if we weigh the linearity threshold of the flow accumulation model by the degree of sloping, the result is a flow network that can reflect the recent geomorphological processes more (Fig. 11).

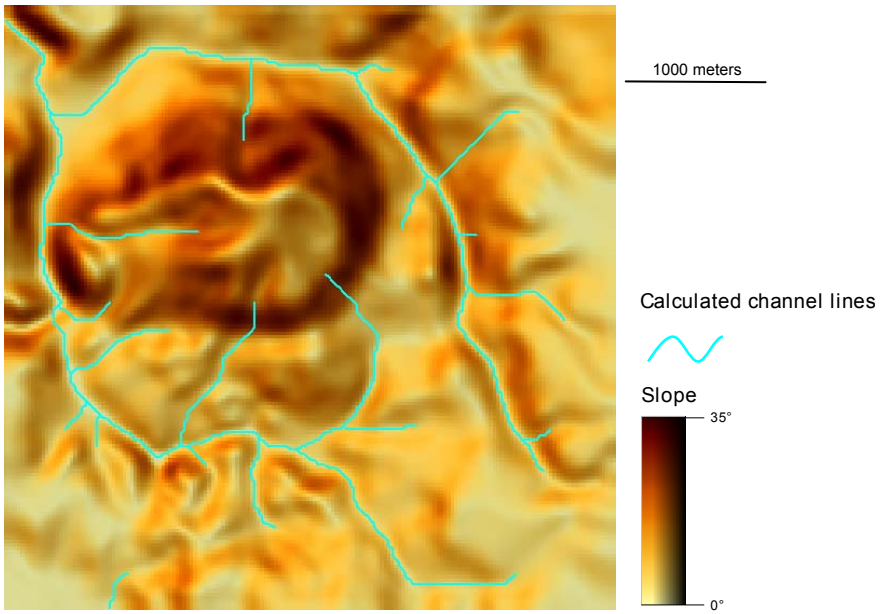

Fig. 11. The channel network determined with the Slope-Area-threshold model

3. Limitations

Models based on flow accumulation thresholds — especially if the degrees of sloping are used for determining thresholds — reflect the potential erosion work caused by the accumulated water. This many times coincides with the actual valleys, however, it is not always possible to determine a single threshold for all subcatchments, since, among other things, it depends on the spatial variability of the climate, relief, geology, vegetation and stage of evolution.

Models which use convergence index thresholds recognise evolved valleys by their shape, disregarding the amount of water running off. In this case the channels in their initial evolutional stages may go unnoticed, and because of the DEM's resolution (usually above 10–30 m cellsize) it does not show convergence. There may be cases when due to a change in the circumstances (e.g.: climate change, capture), we get channel flows at places where the morphological conditions are given by linear runoffs (convergence), however, in reality they do not exist there.

This model also presupposes that if once the accumulated waters become linear runoffs, they keep this characteristic. This assumption is true for the upper parts of catchments with greater relief, but if we also decide to model bifurcation, we must modify the models discussed above to obtain appropriate results.

Those areas may also prove problematic where the movement of water runoff is not primarily determined by relief, because there are strong geological controls on subsurface flow. Such areas are karst landscapes, for example, where waters run dominantly under the surface, or in sandy areas, where the flow directions of ground water show the flow routes.

The results of the model are greatly affected by the spatial resolution of the DEM. The methods discussed so far apply to high-resolution DEMs (10–30 m cellsize). If we increase the cell size, we will be unable to model minor processes and forms. Since the area is more scale

invariant than the other characteristics (e.g.: slope, convergence-index) (Klinkenberg, 1992; Yin and Wang, 1999) we apply the D8 model when analysing global DEMs of larger cellsize (over 100 m). The result can be further improved if we make the best of the fractal nature of drainage system (Mandelbrot, 1982). However, the results of this are still to be improved under development.

4. Applications and results

In this part I will demonstrate the application of the drainage models discussed above through an example. The task is to draw up a water-damage prevention plan for a part of the Pannonhalma hills in Hungary. The main river of the area is the Nagy-Pándzsa. The examined area can be divided into 28 catchments (Fig. 12) — some of these are built up, some are natural areas, but most catchments are situated on areas which are the combinations of these types.

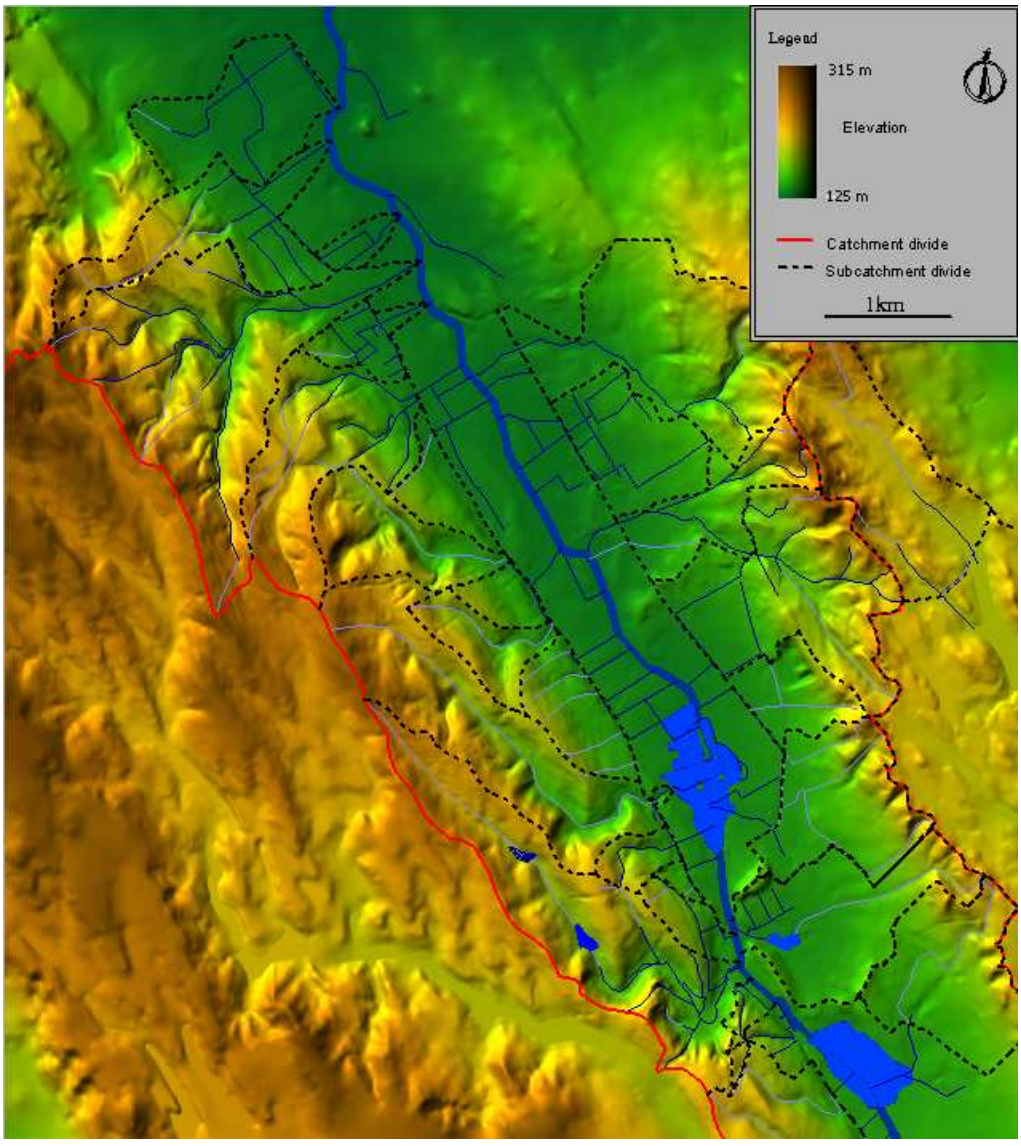

Fig. 12. The DEM and the catchments of the area

The MFD—D8 convergence-threshold index model is used as a drainage model. Ground survey has made it clear that the model cannot give a proper result on its own. The reason for this is that there are numerous artificial — mainly linear — objects on the area that do not appear in the DEM because of the scale of the map used. In some cases the objects that modify the drainage network (e.g.: canals, roads) have so strong effect on the drainage routes that subcatchment divides can be displaced (Fig.13).

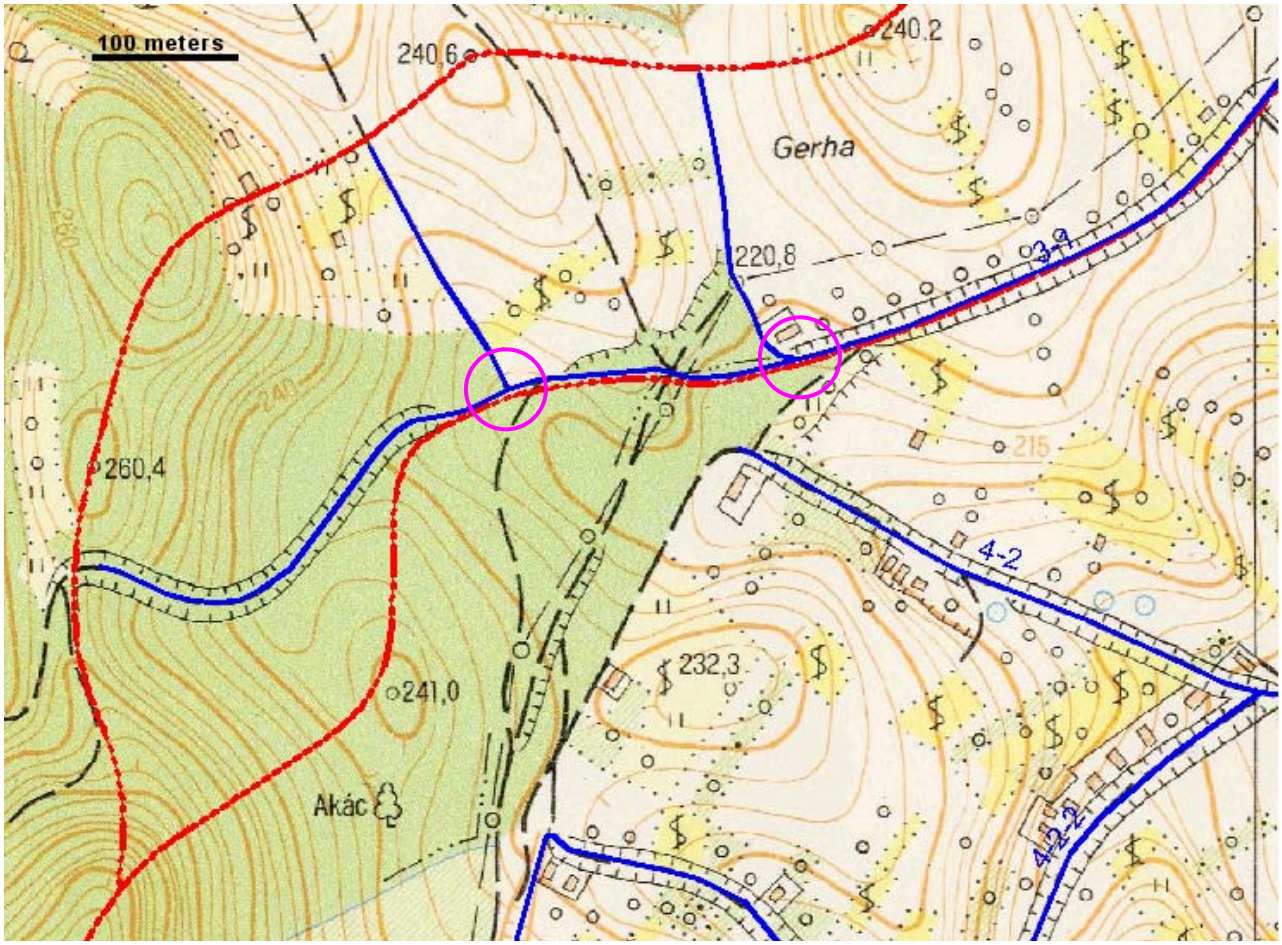

Fig. 13. Capture of a road

To correct these errors we inserted a so called 'drainage forcing' network in the model, which indicates the flow directions of artificial linear objects, too.
The catchment model that we obtain this way topologically shows subcatchments and drainage routes and it makes possible to carry out complex analyses.
The main parts of this complex engineering catchment model are the following:

- DEM
- morphometrical maps (slope, aspect)
- natural and artificial drainage routes
- parameters of artificial drainage routes and their parts (e.g.: locks, culverts etc.)
- bounded catchments, subcatchments
- landuse
- defining authoritative water amount for drainage model

On the basis of experience, automatic drainage network definition can be used on natural areas with good results, but can also prove useful in other cases. I must emphasize the importance of ground survey, since it is essential for creating a correct and reliable model.

ACKNOWLEDGEMENTS

The models and the maps in the paper have been made with SAGA - System for an Automated Geo-scientific Analysis. I would like to thank SAGA workgroup for their advice and work.

REFERENCES

Costa-Cabral, M.C., S.J. Burges, 1994, Digital elevation model networks (DEMON): A model of flow over hillslopes for computation of contributing and dispersal areas: Water Resources Research, v. 30., p. 1681-1692.

Fairfield, J. , P. Leymarie, 1991, Drainage networks from grid digital elevation models: Water Resources Research, v. 27., p. 709-717.

Freeman, T.G., 1991, Calculating catchment area with divergent flow based on a regular grid: Computers and Geoscience, v. 17., p.413-422

Howard, A.D., 1994, A detachment-limited model of drainage basin evolution: Water Resources Research, v. 30, p. 2261-2285.

Howard, A. D., 1997, Badland morphology and evolution: Interpretation using a simulation model: Water Resources Research, v. 22, p. 211–227.

Hutchinson, M. F., 1989, A new procedure for gridding elevation and stream line data with automatic removal of spurious pits, Journal of Hydrology, v. 106, p. 211-232

Jones, N.L., Wright, S.G., Maidment, D.R., 1990, Watershed delineation with triangle-based terrain models: Journal of Hydraulic Engineering, v. 116, p. 1232-1251.

Kirkby, M.J., 1986, A two-dimensional simulation model for slope and stream evolution, in Abrahams, A.D., Hillslope processes: Winchester, Allen and Unwin, p. 203-222.

Kirkby, M. J., 1993, Long term interactions between networks and hillslopes, in: Beven, K., M. J. Kirkby, Channel Network Hydrology: New York, John Wiley and Sons, p. 255-293.

Köthe, R., F. Lehmeier, 1994, SARA System zur Automatischen Relief-Analyse, Benutzerhandbuch, Göttingen

Lea, N.L., 1992, An aspect driven kinematic routing algorithm, in: A.J. Parsons, A.D. Abrahams, Overland flow: hydraulics and erosion mechanics: London, p.147-175.

Mandelbrot, B., 1982, The Fractal Geometry of Nature, San Francisco, W. H. Freeman & Co., p. 468.

Moore, I.D., R. B. Grayson, 1991, Terrain-based catchment partitioning and runoff prediction using vector elevation data: Water Resources Research, v. 27, p. 1177-1191.

Nelson, E.J., Jones, N.L., Miller, A.W., 1994, Algorithm for precise drainage-basin delineation: Journal of Hydraulic Engineering, v. 120, p. 298-312.

O'Callaghan, J. F., D.M. Mark, 1984, The extraction of drainage networks from digital elevation data: Computer Vision, Graphics, and Image Processing, v. 28, p. 328-344.

Peucker, T. K., D. H. Douglas, 1975, Detection of surface-specific points by parallel processing of discrete terrain elevation data: Computer Graphics and Image Processing, v. 4, p. 375-387.

Planchon, O., F. Darboux, 2002, A fast, simple and versatile algorithm to fill the depressions of digital elevation models: Catena, v. 46, p. 159-176.

Tarboton, D. G., 1997, A new method for the determination of flow directions and upslope areas in grid digital elevation models: Water Resources Research, v. 33, p. 309-319.

Tucker, G.E., R.L. Bras, 1998, Hillslope processes, drainage density, and landscape morphology: Water Resources Research v. 34, p. 2751-2764.

Willgoose, G.R., R. L. Bras, I. Rodriguez-Iturbe, 1991, A physically based coupled network growth and hillslope evolution model, 1, theory: Water Resources Research, v. 27, p. 1671-1684.

Modelling Infiltration on Arable Lands

Károly Barta[1]

[1]University of Szeged, Department of Physical Geography and Geoinformatics (barta@earth.geo.u-szeged.hu)

Abstract

Prediction and estimation of soil erosion are of great importance in soil conservation. There are numerous soil erosion models, aimed at realizing these goals. Attempts have been made to adopt some of these to Hungarian conditions as well. The aim of our research was the calibration of the EUROSEM soil erosion model to Hungarian conditions, but because of the algorithmic mistakes of the model, significant problems have been encountered in fitting the modeled and measured data. Hence came the idea to make a new model suited for a new infiltration conception, while keeping the usable equations from the EUROSEM. Individual rainfall events can be modeled on homogeneous plots with the help of this new model.

This article describes the vegetation and infiltration submodel of this newly developed model mentioned above. These are based on exact physical and mathematical equations and can be applied to the majority of arable land conditions, characterized by the presence of a more compacted plough-pan beneath the cultivated upper soil layer with favourable hydrologic properties. The vegetation submodel gives us the temporal distribution of the rainfall reaching the surface as “net rainfall”. This “net rainfall” becomes the input of the infiltration submodel. The infiltration submodel can compute with equalizing the water amounts needed to fill the soil layers until field capacity and maximum soil moisture with definite integrations derived from the Hortonian equation. The model works to determine the following points of time: the initiation of surface runoff, the wetting front reaches the plough-pan, the plough-pan is saturated, the topsoil is saturated. All intervals between these moments can be ordered different functions of the infiltration and runoff. The model was programmed in Maple V.

Keywords: soil erosion, modeling, Hortonian infiltration

1. INTRODUCTION

Water erosion on agricultural lands is a global problem. The natural erosion is only 0.1-0.3 t/ha as contrasted with the so-called accelerated erosion caused by the permanent land use which can be 6-100 times greater (GOUDIE, A. 1995). Erosion exceeding the rate of soil formation leads to serious economical and ecological problems. The direct measurement of

erosion includes expansive and difficult methods, therefore dozens of infiltration and erosion models are worked out which attempt to describe more or less exactly the erosional processes (WISCHMEIER, W. H. et al. 1978, DE ROO, A. P. J. et al. 1992, GRAYSON, R. B. et al. 1992, MORGAN, R. P. C. et al. 1993, FLANAGAN, D. C. 1994, YOUNG, R. A. et al. 1994, SCHRÖDER, R. 2000). Unfortunately, the measurement of numerous input parameters influencing erosion is not without problems, and even if any parameters can be measured accurately, their spatial and temporal variability yields further uncertainties. Consequently, it is necessary to set up standards for each model, which include the typical values of parameters depending on soil texture or vegetation type. These tables based on thousands and thousands measured data have limited spatial usability. They can be used only in similar geographical settings to which they were originally applied. The basic condition to use the models in other areas is the adoption of these tables, or nomograms, as the calibration of the model is called, for local conditions.

More and more models are adopted to different regions in order to estimate any changes in erosion conditions (e.g. QUINTON, J. N. 1997). There are some models (e.g. USLE, WEPP, EPIC) which were calibrated in Hungary and they have been used for many years in our country as well (KERTÉSZ, Á. et al. 1997, HUSZÁR, T. 1998, KERTÉSZ, Á. et al. 2000, CENTERI, CS. et al 2003). The first step of this research was the calibration of the EUROSEM soil erosion model to Hungarian conditions. It is an event based dynamic model for plots and small catchments worked out for European Countries (MORGAN, R. P. C. et al. 1998).

During the process of the calibration it was shown that the EUROSEM has got some algorithmic, conceptional and other problems. Fitting the modeled and measured data was practically impossible (BARTA, K 2001). Hence came the idea to prepare a new model based on the EUROSEM. The basic concept of the new model is that it should avoid the problems encountered in the EUROSEM while keeping the usable part of the same model. So the major aim of the present work was to develop a dynamic mathematical model, which is suitable to model the effect of a rainfall event on a plot to the infiltration, runoff and erosion.

2. THE STRUCTURE OF THE NEW MODEL

2.1. The Basic Concept

The most typical conditions occurring on an arable land were chosen as the theoretical basis of the new model, namely where the upper part of the soil consists of two different layers: the cultivated topsoil and the more compacted plough-pan beneath. They can have different physical and hydrological properties in the model. This first version of the model can be used only in the case of permanent rainfall intensity and deep soil water table with no effect to the infiltration. The model consists of four submodels (Fig.1.):

1. The vegetation submodel describes the way of the rainfall until the surface (direct throughfall, leaf drainage, interception storage). The newness of this part of the model is that it can avoid the main algorithmic problem of the EUROSEM, taking into account the maximum interception storage of the vegetation in good sense.

2. The infiltration submodel can show the temporal distribution of the surficial rainfall between the infiltration and runoff. It was founded on absolutely new bases. The most important features of the submodel are the following:

- The infiltration is determined by the characteristics of the different soil layers, for e.g. saturated/unsaturated hydraulic conductivity, soil moisture, different water capacities.
- Only measurable or calculable soil parameters are used almost exclusively as an input.
- The measurement methods to each applied parameters are fixed and ordered.
- The hydraulic conductivity for each soil layer is described by the Hortonian function (HORTON, R. E. 1933).
- Based on the Hortonian equation, the saturation and infiltration of the different soil layers is characterized via mathematical functions.

3. The runoff sub-model describes the runoff intensity in space and time. It is based on the EUROSEM's equations.

4. The erosional part of the model was adopted from the EUROSEM as well. The sediment yield is given by the product of the water runoff and the sediment concentration (MORGAN, R. P. C. et al. 1998).

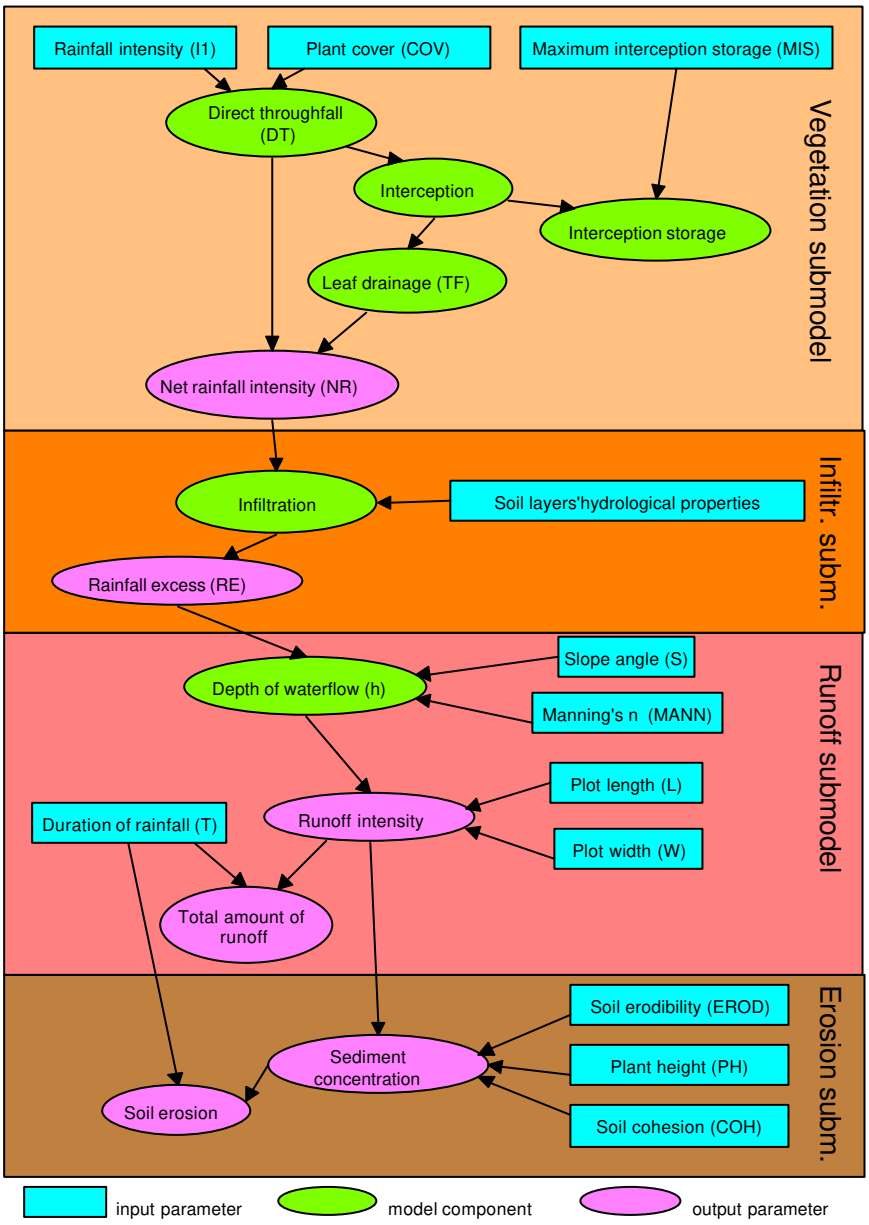

Fig.1. The algorithm of the model.

The first two submodels are described in the following parts of this article.

2.2. The Vegetation Submodel

The vegetation submodel describes the way of the rainfall until the surface. Besides the direct throughfall, a part of the rain remains on the leaves of plants filling up its interception storage. The other part forms the throughfall via the leaves. Thus, this submodel needs the following input parameters:

1. Plant cover (COV)
2. Maximum interception storage (MIS, mm)

There are lots of relationships explaining the temporal process of vegetation storage capacity fill up (WISCHMEIER, W. H. et al. 1978, KIRKBY, M. J. et al. 1980, MORGAN, R. P. C. et al. 1993, BERGSMA, E. 1996). Here we used the modified version of the equation derived from the EUROSEM (MORGAN, R. P. C. et al. 1998):

$$NR(t) = I1*(1-e^{-I1*t/(MIS*COV)}) \qquad (1)$$

where I1 is the rainfall intensity in mm/min,
t is the time passed from the start of rainfall (min)
NR is the "net rainfall intensity" reaching the surface (mm/min).
NR(t) means the output of the vegetation submodel and the input of the infiltration submodel.

2.3. The Infiltration Submodel

This submodel gives us the distribution of the net rainfall intensity between infiltration and runoff. The input parameters characterizing the physical and hydrological properties of both the topsoil and the plough-pan are summarized in Table 1. From this stage on *1* in subscript will highlight the parameters of the topsoil, and *2* in subscript will signify those of the plough-pan.

Table 1: Soil properties used as input parameters to the infiltration submodel

Parameter	***Mark***	***Unit***	***Notes***
Thickness of the layer	D	cm	
Maximal water content	P	v/v	
Field capacity	KP	v/v	
Gravity pores	GP	v/v	GP=P-KP
Initial average soil moisture	M	v/v	
Saturated hydraulic conductivity	K_c	mm/min	
Hortonian function of hydraulic conductivity	K(t)	mm/min	$K(t)=K_c+(K_0-K_c)e^{-At}$
(K_0: initial water absorption (mm/min), A: constant characteristic for the soil layer)			

With these parameters in hand the volume of water needed to fill up the pores of the given soil layer between the initial soil moisture and field capacity or between the field capacity and maximum soil moisture can be estimated using the following equations:

$$KT = 10*D*(KP-M) \qquad (2)$$

$$GT = 10*D*(P-KP) = 10*D*GP \qquad (3)$$

where KT is the amount of water necessary for reaching the field capacity from the initial soil moisture and GT is the amount of water necessary for reaching the state of full saturation from the field capacity. Both of them are in mm.

The saturation of the topsoil is carried out through the following four "significant moments" (Fig.2):

T_1 marks the place of the intersection of the NR(t) and K_1(t) functions, when the values of the net rainfall become greater than the water absorption of the topsoil. This is the initiation of runoff.

T_2 marks the moment when the topsoil reaches its field capacity corresponding to the initiation of the plough-pan's absorption.

T_3 means the start of the saturation of the gravity pores in the topsoil namely the absorption of the plough-pan decreases under the hydraulic conductivity of the topsoil then.

T_4 is the moment of the full saturation of the topsoil.

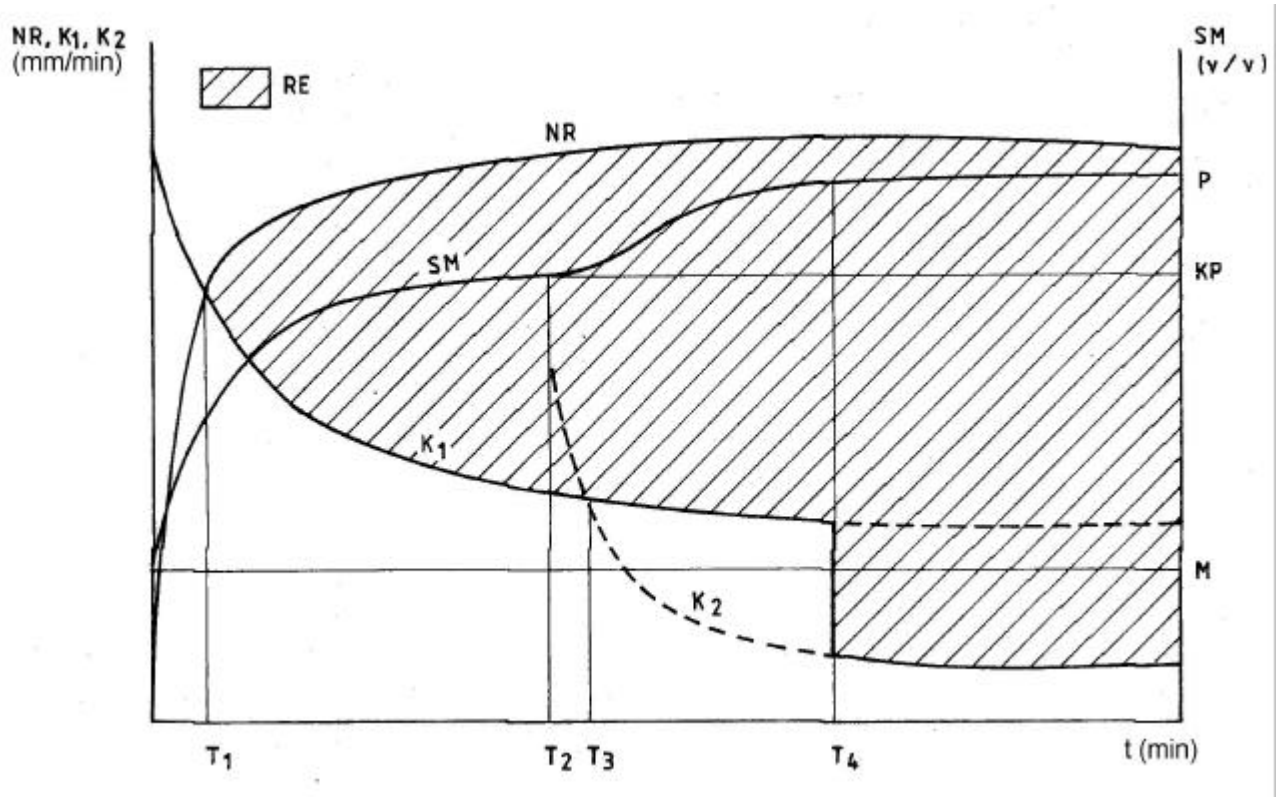

Fig.2. The saturation of the topsoil showing the "significant" moments. SM: moisture of the topsoil, RE: the uninfiltrated part of the net rainfall in mm/min (called rainfall excess, see later)

T_1 can be calculated by equalizing the Hortonian function of the topsoil with the net rainfall intensity:

$$NR(t) = K_1(t) \qquad (4)$$

T_2 is calculated by equalizing the amount of water necessary for reaching the field capacity (KT_1) with the function $K_1(t)$ integrated for the interval of (0;x) where the determination of the unknown x gives us T_2:

$$KT_1 = \int_0^x K_1(t)dt(= CK_1(x)) \qquad (5)$$

where CK_1 marks the cumulative amount of water infiltrated into the topsoil.

The existence of T_3 depends on the extent of differences between the hydrological properties of the two soil layers. Sometimes the initial water absorption of the plough-pan is lower than the hydraulic conductivity of the topsoil even at T_2. In this case defining T_3 makes no sense. In other cases T_3 can be determined by the solving the following equation:

$$K_1(t) = K_2(t-T_2) \qquad (6)$$

Water penetrating downwards starts to fill up the macro-pores in the topsoil at the moment T_3. Consequently T_4 can be calculated by equalizing the amount of water necessary for reaching the maximal water content from the field capacity (GT_1) with the following term:

$$\int_{T_3}^{x} K_1(t)dt - \left[\int_{T_2}^{x} K_2(t-T_2)dt - \int_{T_2}^{T_3} K_1(t-T_2)dt \right] = GT_1 \qquad (7)$$

where the first term is the total amount of water infiltrated into the soil from T_3 and the second term gives the part of the previous one that penetrated into the plough-pan.

The part of the net rainfall intensity that can not infiltrate into the soil gives the available amount of water for runoff. This is the most important output parameter of the infiltration submodel referred to as the “rainfall excess” (RE, mm/min – see Fig.2.). Based on the knowledge of the significant moments, the function RE can be given by different terms for different intervals:

$$RE(t) = 0, \quad \text{if } 0 = t = T_1 \qquad (8)$$

$$RE(t) = NR(t)-K_1(t), \quad \text{if } T_1 = t = T_4 \qquad (9)$$

This second equation means that the hydraulic conductivity of the topsoil can determine runoff until T_4. After T_4 the plough-pan’s properties play the most important role in runoff:

$$RE(t) = NR(t)-K_2(t-T_2) \qquad (10)$$

The difference between equations (9) and (10) causes a sudden change in rainfall excess which has no reality in the natural processes on arable lands. In order to remove this breaking point at T_4, the function RE was linearized between $0.95*T_4$ and $1.05*T_4$. The rightness of the choice of the interval's length should be controlled by field measurements in the future.

The rainfall excess will be one of the most important input parameters of the runoff submodel.

2.4. Technical Supports

These two submodels forming the basis of this article were programmed in Maple V. Maple gives us both the equation of function RE and its plotted graph. The runoff and erosion submodels can be run – suitably for its similarity of the EUROSEM – under the software of the EUROSEM. The main technical problem is to convert the intensity values of the rainfall excess into the data of the cumulative rainfall used in the EUROSEM's rainfall file. This last one can suppose only such a cumulative function which consists of linear sections, meaning that its derivative must be a step function.

Thus in the first step the function RE was integrated in order to make a cumulative function. Secondly it was divided into 4 and 2 linear sections between T_1 and T_2 and between T_4 and the end of the rainfall in Maple. Parallel with this, both the saturated hydraulic conductivity and the maximum interception storage of the vegetation as input parameters in the EUROSEM rainfall file must have zero values.

3. DISCUSSION

The model presented in this article is only an initial version of a model that will be suitable for a much more wide-scale use than this one. The main directions of the development can be summed up as follows:

- The embedment of the subsurface runoff that starts at the top of the plough-pan after T_3 into the model
- The use of even more input parameters to increase the accuracy and the reality of the model,
- The expansion of the applicability of the model to unsteady rainfall conditions as well,
- The testing of the model with comparison real measured and simulated data.

The main technical challenge is the programming of the model within a frame of any uniform software.

Naturally, it is possible to modify the model where there seem to be great differences between the real process and the algorithm of the model during the testing phase.

4. SUMMARY

The newly presented dynamic mathematical model is suitable to calculate runoff and erosion in plot scale. This first version can be used in the case of permanent rainfall intensity and assuming a layered soil profile with cultivated topsoil and more compacted plough-pan. The theoretical basis of the new model comes from the determination of some "significant"

moments during the infiltration with the help of differential equations. However, further developments are required to test and refine the model in the future.

5. REFRENCES CITED

BARTA, K. 2001: A EUROSEM talajeróziós modell tesztelése hazai mintaterületen. In: A földrajz eredményei az új évezred küszöbén. Magyar Földrajzi Konferencia. Szeged, 2001. október 25-27. (CD)

BERGSMA, E. (ed.) 1996: Terminology for soil erosion and conservation. Wageningen.

CENTERI, CS. – PATAKI, R. 2003: A talajerodálhatósági értékek meghatározásának fontossága a talajveszteség tolerancia értékek tükrében. Tájökológiai Lapok 1/2. pp. 181-192.

DE ROO, A. P. J. – RIEZEBOS, H. Th. 1992: Infiltration Experiments on Loess Soils and Their Implications for Modelling Surface Runoff and Soil Erosion. Catena 19, pp. 221-239.

FLANAGAN, D. C. (ed.) 1994: Water Erosion Prediction Project. Erosion Prediction Model v94.7 User Summary. USDA-ARS NSERL, West Lafayette – USA.

GOUDIE, A. 1995: The Changing Earth. Rates of Geomorphological Processes. Blackwell Oxford, pp. 131-139.

GRAYSON, R. B. – MOORE, I. D. – McMAHON, T. A. 1992: Physically Based Hydrologic Modeling 1-2. Water Resources Research 26-28, No. 10, pp. 2639-2666.

HORTON, R. E. 1933: The role of infiltration in the hydrologic cycle. Trans. Am. Geophys. Union 14. pp. 446-460.

HUSZÁR, T. 1998: A talajerózió térképezése és modellezése magyarországi mintaterületeken térinformatikai módszerekkel. PhD értekezés tézisei. Budapest.

KERTÉSZ, Á. – RICHTER, G. – SCHMIDT, G. – BRAUNSCHWEIG, W. – HUSZÁR, T. – LÓCZY, D. – SCHÄFER, A. – MÁRKUS, B. – VARGA, G. – HENZLER, B. 1997: The Balaton Project. ESSC Newsletter 2-3. Bedford. p. 37.

KERTÉSZ, Á. – HUSZÁR, T. – TÓTH, A. 2000: Soil Erosion Assessment and Modelling. In: Physico-geographical Research in Hungary (ed: Kertész, Á. et al.). Studies in Geography in Hungary 32. Geographical Research Inst. HAS, Budapest. pp. 63-74.

KIRKBY, M. J. – MORGAN, R. P. C. (ed.) 1980: Soil Erosion. J. Wiley & Sons, New York.

MORGAN, R. P. C. – QUINTON, J. N. – RICKSON, R. J. 1993: EUROSEM: A User Guide. Silsoe College.

MORGAN, R. P. C. – QUINTON, J. N. – SMITH, R. E. – GOVERS, G. – POESEN, J. W. A. – AUERSWALD, K. – CHISCI, G. – TORRI, D. – STYCZEN, M. E. 1998: The European Soil Erosion Model (EUROSEM): A Dynamic Approach for Predicting Sediment Transport from Fields and Small Catchments. Earth Surface Processes and Landforms 23. pp. 527-544.

QUINTON, J. N. 1997: Reducing predictive uncertainty in model simulations: a comparison of two methods using the European Soil Erosion Model (EUROSEM). Catena 30. pp. 101-117.

SCHRÖDER, R. 2000: Modellierung von Verschlämmung und Infiltration in landwirtschaftlich genutzen Einzugsgebieten. Bonner Geographische Abhandlungen 101. Asgard-Verlag, Sankt Augustin

YOUNG, R. A. – ONSTAD, C. A. – BOSCH, D. D. – ANDERSON, W. P. 1994: Agricultural Non-Point-Source Pollution Model (AGNPS). User´s Guide (Version 4.03). USDA, Agricultural Research Service, Washington.

WISCHMEIER, W. H. – SMITH, D. D. 1978: Predicting Rainfall Erosion Losses. Agricultural Research Service Handbook No. 282. United States Department of Agriculture, Washington.

Interpretation of spatial distribution of sediment toxicity data

Nóra Kováts[1], Gábor Borbély[1], Imre Magyar[1], Zsuzsanna Szép[1], Gábor Paulovits[2] and Piroska Pomogyi[3]

[1]University of Veszprém, School of Environmental Engineering and Chemical Technology, Veszprém, Hungary. E-Mail: toxlab@almos.vein.hu

[2]Balaton Limnological Research Institute of the Hungarian Academy of Sciences, Tihany, Hungary. E-Mail: paulo@tres.blki.hu

[3]West Transdanubian Water Authority, Dept. Kis-Balaton, Keszthely, Hungary. E-Mail: pomogyi.piroska@nyuduvizig.hu

Abstract

Sediment plays a central role in ecosystem processes. Contaminated sediment may pose a serious risk, affecting ecosystem health in many ways, seriously damaging restoration and rehabilitation measures. A wide variety of methods are available by which sediment contamination can be assessed, in most cases chemical and biological methods are combined. While chemical analysis is focusing on the potential exposure, ecotoxicity testing and biological survey are estimating the potential and actual ecological effects. None of these methods alone are able to provide a firm basis for environmental decision making. In this study the potential of spatial analysis of environmental data to characterize contamination distribution, to identify hot spots and to link toxicity data to contamination concentration/sources is illustrated. For demonstration we have selected two case studies, both are of practical importance.

Keywords: sediment contamination, toxicity assessment, ToxAlert, risk mapping

1. INTRODUCTION

Sediment is a key structural and functional component of any aquatic ecosystem. Toxics in the sediment play a secondary source of contamination, posing risk to aquatic biota long after the primer source had disappeared. Toxic contaminants can be present in the sediment in many forms: they can be bound to the sediment particles and can be dissolved in the so-called pore water. Therefore, biotic components of the ecosystem can be affected in a different way. Firstly, sediment-dwelling organisms can be exposed to toxics directly, in other word, they are in direct contact with contaminants. Some sediment-dwelling taxa play an important role in keeping the ecosystem healthy: for example, larvae of midges (family Chironomidae) live in the sediment, and when they emerge they remove all the nutrients from the lake they have built in. Fish feeding on

such organisms might be exposed both directly and indirectly. Indirect exposure means consuming contaminated organisms. Plants rooting in contaminated sediment might accumulate toxics, contributing to exposure pathways. Toxics being present in the pore water might escape to the water, posing risk to not only those organisms which are in contact with the sediment but for all elements of the ecosystem.

It seems obvious that mapping sediment contamination is a very important tool either for assessing environmental health or for establishing remediation measures. Environmental authorities might need to rank contaminated sites and to establish target remediation objectives for dredged material.

Standard analytical methods are available to provide an accurate measurement on the concentration of a given contaminant (exposure assessment). On the other hand, toxicity tests are focusing on the potential effect of the contaminant or of the contaminated medium. However, either analytical tools or toxicity tests alone might fail to accurately determine ecosystem health: analytical measurements do not give any information on the bioavailability of the contaminant in question while toxicity testing gives an overall measure of the ecotoxicity of the medium, not distinguishing natural and anthropogenic factors. In general, if toxicity is occurring, measured values should be related to exposure or to some indicative measure of exposure (e.g. MacDonald and Ingersoll, 2002). Seemingly, the simplest way of doing that is to calculate correlation between contaminant concentrations and toxicity. An alternative approach can be to determine the relationship between the occurrence of toxicity (e.g. toxicity measured is well above levels considered significant) and sources of contaminants (such as effluents, spills, etc.) (Suter, 1996).

In the decision making process communication of the results is of crucial importance. Risk is most often reported as a single value, neglecting the spatial nature of risk. Risk assessment must deal with a diverse set of data, including multiple contaminants sampled from multiple locations at different intervals. However, it is very difficult to summarise and interpret these data in a format applicable for decision-makers. Communication may be enhanced by spatial analysis and visualization (Bertazzon et al., 2000). In this study the potential of spatial analysis of environmental data to characterize contamination distribution, to identify hot spots and to link toxicity data to contamination concentration/sources is illustrated. For demonstration we have selected two case studies, both are of practical importance.

2. TOXICITY ASSESSMENT IN THE SÓS-TÓ OF SZÉKESFEHÉRVÁR AS A PRE-RECONSTRUCTION TOOL

Sós-tó (the name means Salt Lake) is a degraded wetland in Székesfehérvár. Its degradation has been partly caused by drying out, partly by uncontrolled sewage load which had been piped till March 2000. Due to the sewage effluent significant sediment disposal had occurred and presence of diverse pollutants can be expected. On behalf of the Major's Office of Székesfehérvár considerable efforts have been made to take rehabilitation measures. 4 alternative concepts have been elaborated for the complex restoration of the area, partly to restore its wetland functions and partly to ensure its wise use (ForEnviron, 2002). The common element of all concepts is to raise water level by using external water supply, restoring a wetland with open water. As sediment contamination might damage the success of the rehabilitation, our basic aim was to make an ecological risk assessment to get a complex view about what risk sediment

contamination might pose to the success of any future rehabilitation work, using different parameters to characterise contamination level.

2.1 Analysis of the sediment samples

Sediment samples were collected in two series. The first series was collected on 30th September, 2003, at this time the lake was completely dry (Fig. 1.). The second series was collected on 7th April, 2004, after a rainy winter and spring period the lake was under water (Fig.2.). GPS coordinate were recorded on the field using an e-trex Vista GPS.

Fig.1. The Salt Lake in autumn 2003 ….

Fig.2. … and in spring 2004.

The first series was collected for screening purposes, and only toxicity was measured. In spring 2004 a more comprehensive study was initiated, and besides

toxicity, other environmental parameters were measured such as BOD, COD, TOC, TSS and NO_3^--N.

Toxicity of the sediment samples was measured using ToxAlert®100 luminometer. The test uses bacterial bioluminescence which is a rapid indicator of the metabolic status and of the viability of the cell. The enzyme involved in the process is bacterial luciferase. A toxic substance will cause changes in some cellular structures or functions such as the electron transport system, cytoplasmic constituents or the cell membrane, which are directly reflected in a decrease in bioluminescence.

During the test luminescent organisms are exposed to aqueous samples, and the light output of the luminescent bacteria is measured before and after they have been challenged by a sample. A difference in light output between the sample and the control is attributed to the toxicity of the sample on the organisms. The ToxAlert®100 luminometer calculates the inhibition effect (H_t) of the samples automatically in % values.

Although some authors question the relevance of the test organism, being a marine bacterium, sensitivity and applicability to test sediment toxicity is widely demonstrated and accepted (e.g. Guzzella et al., 1993, Burton et al., 2001a). However, as it is the case with all ecotoxicological tests, sensitivity varies according to the contaminant. It is partly due to the acute nature of the test: short term assays may not be able to detect the toxicity of high K_{ow} compounds as they are more slowly desorbed (Burton et al., 2001b). The test is more often recommended for screening purposes (e.g. Bennett and Cubbage, 1992).

BOD, COD, TOC, TSS and NO_3^--N were measured by a *Secomam* Pastel-UV which is a portable UV analyser for water quality. It is a rapid, multiparametric measuring set. The traceability of the measured components is based on the analysis of UV absorption spectra of the samples.

For toxicity assessment and for BOD, COD, TOC, TSS and NO_3^--N analyses aquaeous solutions had to be used. Elutriates were prepared by Hungarian Standard MSZ 21470/2-81:1982.

2.2 Results of sediment contamination assessment

Toxicity of the first series of sediment samples collected in autumn 2003 is shown in Table 1.

Table 1: Toxicity measured in autumn, 2003.

Number of sediment sample	Inhibition %		Number of sediment sample	Inhibition %	
	15 min	*30 min*		*15 min*	*30 min*
1	9.20	22.25	7	2.05	7.15
2	8.80	10.45	8	-0.20	3.85
3	-13.35	-9.20	9	-1.75	-6.50
4	6.70	5.75	10	4.50	6.25
5	-3.30	-0.70	11	11.05	13.95
6	7.70	12.90	12	1.20	2.90

Table 2 gives an overview of sediment samples collected in spring 2004, indicating all environmental parameters measured.

Table 2: Contamination of sediment samples collected in spring, 2004.

Number of sediment sample	Inhibition %	NO_3^-- N	TSS	COD	BOD_5	TOC
	30 min	*mg/l*				
E1	60.55	49	430	650	250	190
E2	54.85	46	460	560	130	100
E3	58.20	52	470	670	230	180
E4	61.15	50	950	2100	1200	950
E5	57.05	53	630	830	240	180
E6	61.50	48	500	610	140	100
E7	59.75	48	520	670	180	140
E8	59.40	48	550	750	250	190
E9	55.00	48	500	620	150	110
E10	60.40	47	590	870	310	240
E11	58.90	52	260	700	460	380
E12	56.00	47	580	1000	470	370
E13	60.90	51	450	650	220	170
E14	51.65	48	470	670	230	180
D1	40.30	46	310	380	90	100
D2	48.80	48	770	1080	360	280
D3	47.90	48	460	570	130	100
D4	51.85	50	230	390	170	140
D5	41.10	43	190	230	50	100
D6	46.35	42	380	470	110	100
D7	53.75	25	510	630	160	110
D8	23.65	28	250	310	70	100
D9	40.30	24	570	930	410	320
D10	45.75	24	400	480	11	100
D11	45.60	23	330	480	170	130
D12	46.80	24	380	460	100	100
D13	58.70	25	1700	3850	2250	1800
D14	45.20	77	210	1580	1160	94

Toxicologists generally call a sample toxic when the bioluminescence inhibition exceeds 20%. The data below 0 means the sample had stimulating effect on the test organisms.

2.3 Interpretation of temporal distribution of data measured

There are striking differences between the two series of measurement. As it was mentioned already, in autumn 2003 the area was completely dry, but in spring 2004 it was under water. The fact that practically no toxicity was detected during the first measurement and in contrary, during the second measurement bioluminescence inhibition was well above 20% may be explained by a shift towards anaerobic conditions. It is also a possible explanation that toxic compounds had been dissolved.

2.4 Interpretation of spatial distribution of data measured

The measured data were pictured by Surfer8. It's a very user-friendly contouring and 3D surface mapping program by *Golden Software*. Isocline maps produced are shown in Fig. 3.

Fig.3(a) shows the result of 2003 autumn assessment, when sampling was made under dry conditions. The 2004 spring assessment simulates post-restoration conditions much better, thus we make our conclusion on the basis of the second series of measurements. At the first glance effect (toxicity) and exposure (BOD_5, COD, TOC, TSS, NO_3^--N) do not show a clear correlation. Toxicity reflected as bioluminescence inhibition shows a rather uniform spatial distribution in the northern part of the lake (Fig.3(b)). However, toxicity itself is an aggregate parameter, reflecting the so-called matrix effect (Overton et al., 1997). Natural processes might also be responsible for the presence of toxic agents. For example, sulphur, which is produced during the microbial oxidation of sulphide, can be found in anaerobic sediments (Jacobs et al., 1992). On the other hand, most of the analytically derived values of contaminants (BOD_5, COD, TOC, TSS) are in good correlation with each other, delineating the most polluted zones as can be seen in Fig.3(d), (e), (f) and (g). Creating a map where information regarding both exposure and effect is visualised, overlapping zones will clearly identify hot spots. Such a map can be seen in Fig.3(h). This map was created by aggregating exposure and effect data. Considering the history of the area, hot spots are probable sinks of organic pollution, posing risk to the area even after sewage effluent was terminated.

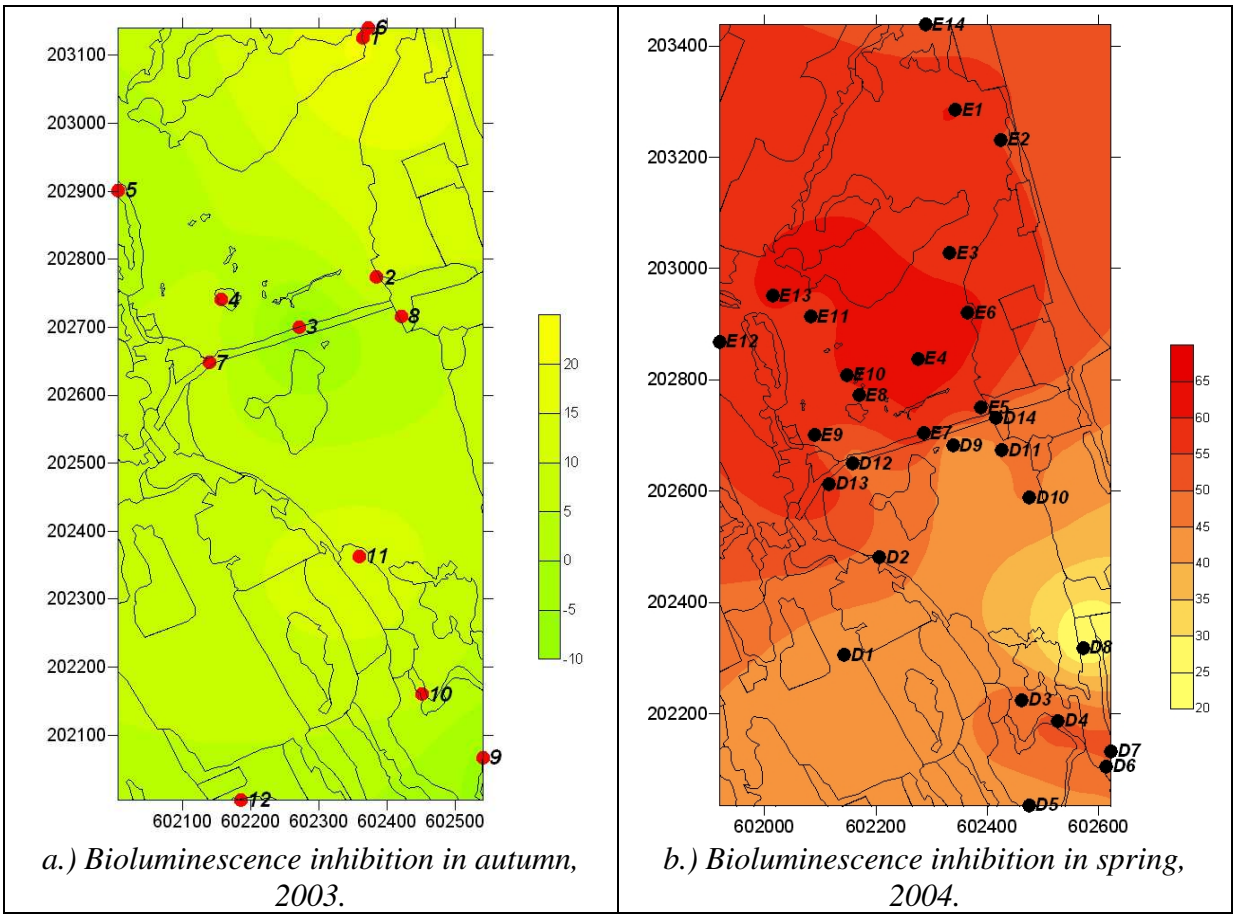

a.) Bioluminescence inhibition in autumn, 2003.

b.) Bioluminescence inhibition in spring, 2004.

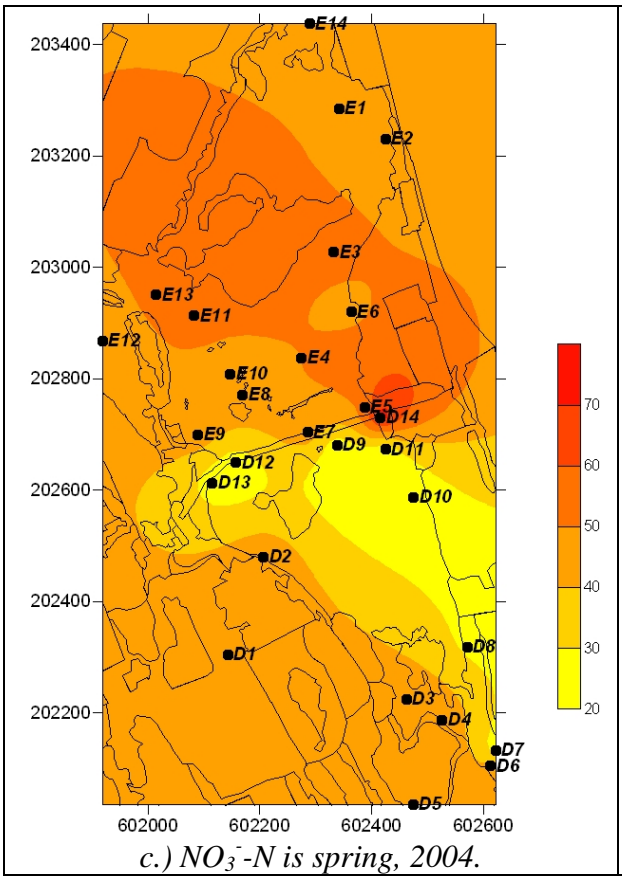

c.) NO_3^--N is spring, 2004.

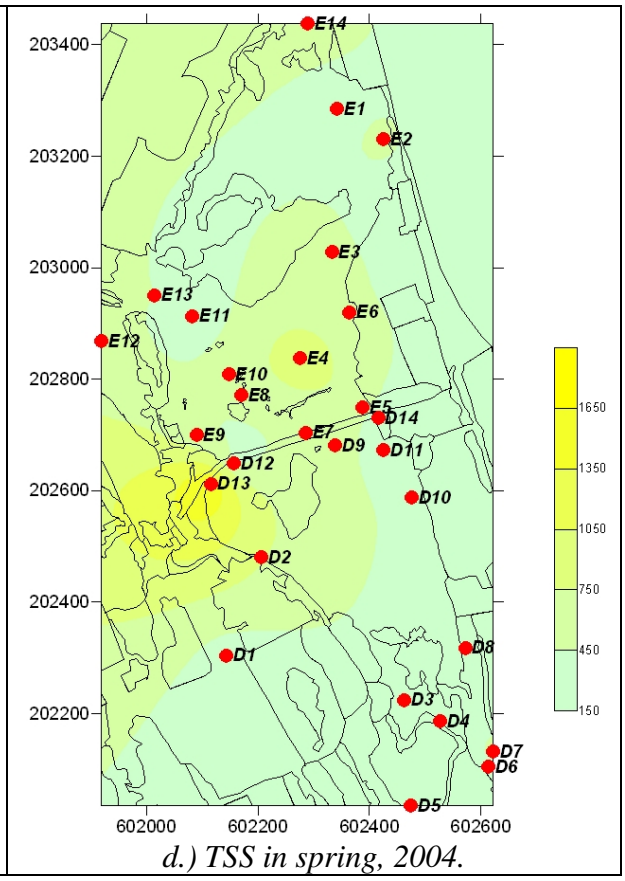

d.) TSS in spring, 2004.

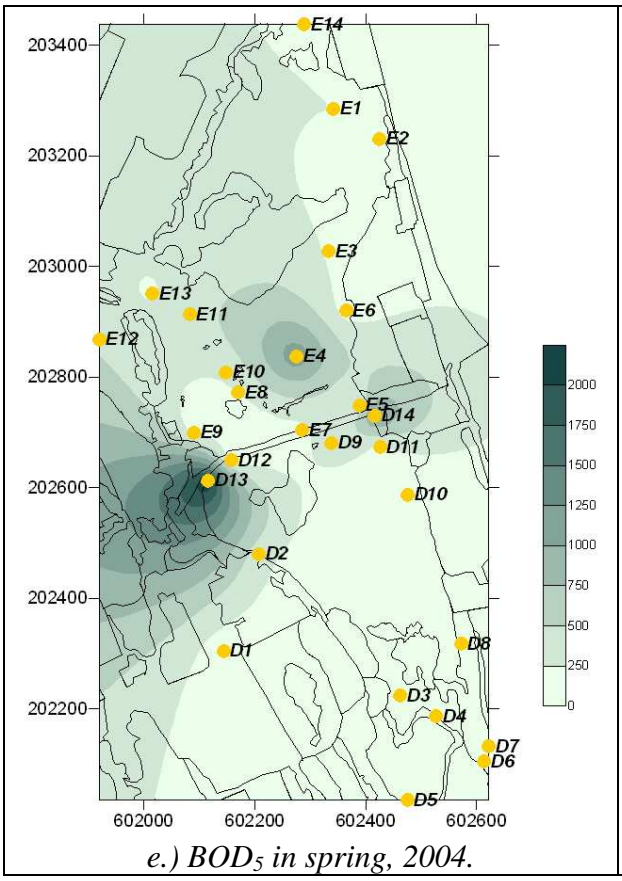

e.) BOD_5 in spring, 2004.

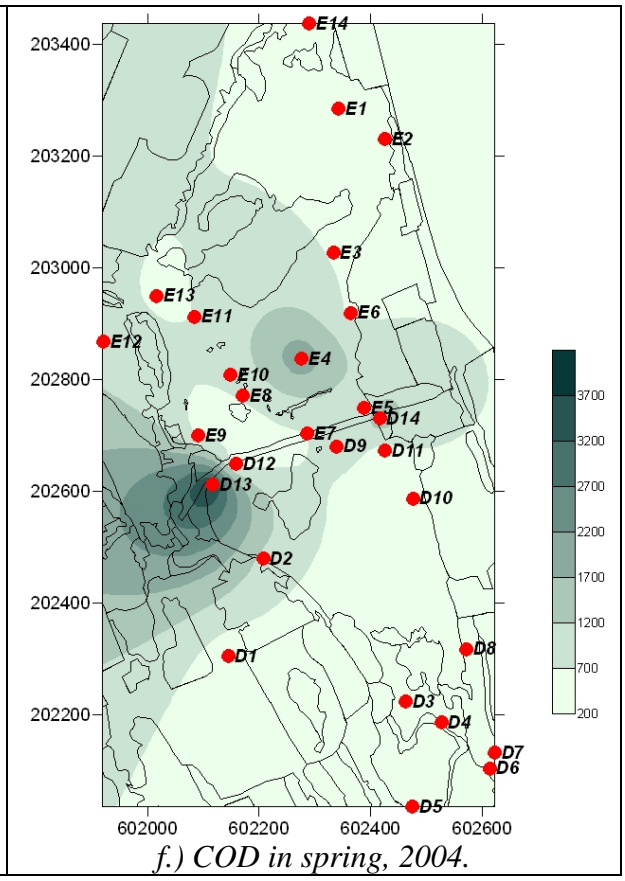

f.) COD in spring, 2004.

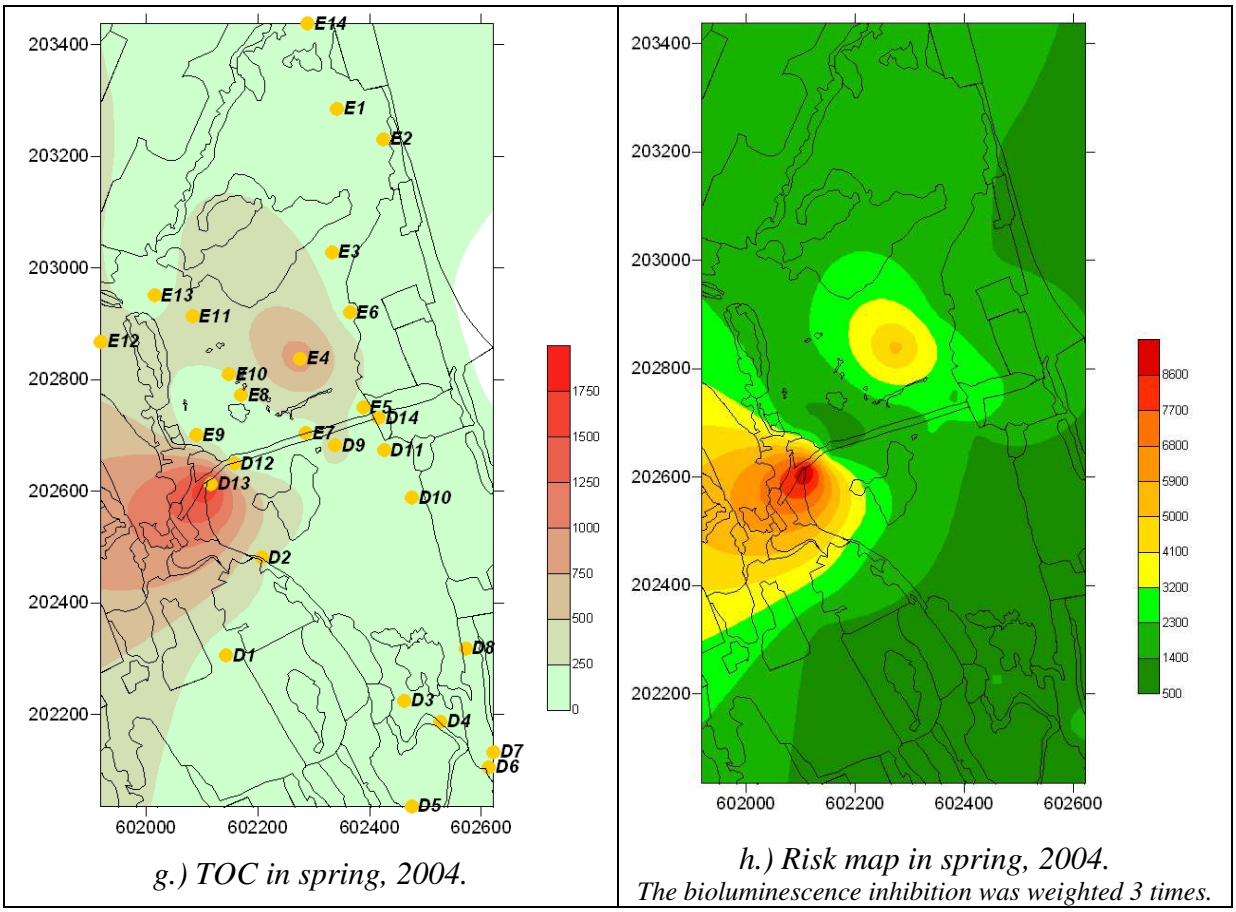

g.) TOC in spring, 2004.

h.) Risk map in spring, 2004.
The bioluminescence inhibition was weighted 3 times.

Fig. 3. Contour maps

The difference between the nitrate-nitrogen and the other maps can be explained by the adsorption range of the Pastel-UV.

3. MAPPING TOXICITY IN THE KIS-BALATON WATER PROTECTION SYSTEM

Lake Balaton and the Kis-Balaton Water Protection System are situated in the western part of Hungary (Fig. 4.). Main function of the system is the protection of the water quality of Lake Balaton, by retenting most of the nutrients and suspended solids carried by River Zala and other, small watercourses. The system is in fact made up of two reservoirs. The first part, the Hídvégi Pond was completed in 1985. The second part, the Fenéki Pond has been partially operating since 1992.

Between 1986 and 1997 the first reservoir, Hídvégi Pond retained app. 78 000t of suspended solids, 290 t of TP, in which 250 t of phosphate and 800 t of TN (Tátrai et al., 2000). The second reservoir, Fenéki Pond retains app. 75% of suspended solids coming from the first reservoir. However, these figures were calculated on the basis of input carried by River Zala regarded as a point pollution source. Load carried by small watercourses and other, mostly non-point sources such as agricultural runoff were not taken into consideration.

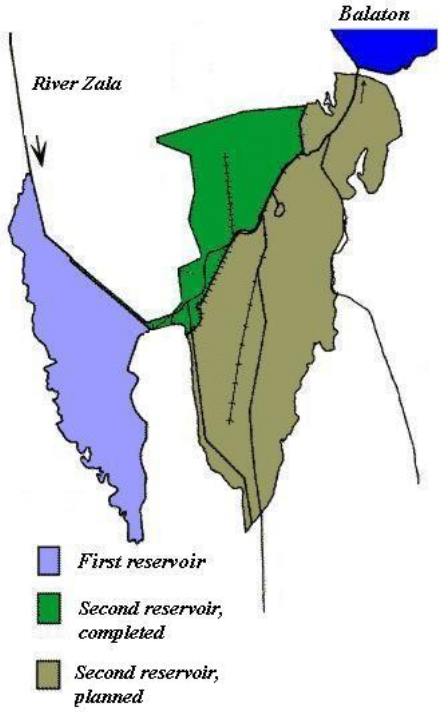

Fig.4. Location of Lake Balaton and the Kis-Balaton Water Protection System.

3.1 Analysis of the sediment samples

Fig.5 shows the sampling spots in the second reservoir. As a baseline map we used the digital ortophoto provided by the West Transdanubian Water Authority, Dept. Kis-Balaton. The infrared imagery reflects vegetation conditions: the more intense the red colour is, the more intense photosynthetic activity is attributed.

Toxicity of the samples was determined using ToxAlert as described above. Bioluminescence inhibition values measured are given in Table 3.

Table 3: Toxicity of sediment samples collected in the Kis-Balaton Water Protection System.

Number of sediment sample	Inhibition %	
	15 min	*30 min*
1	75.05	72.63
2	59.05	54.90
3	37.15	34.35
4	45.25	69.70
5	71.78	65.37

3.2 Spatial distribution of toxicity data measured

Toxicity values are also indicated in Fig.5. In the case of sampling spots 1-2, 4-5, in order to characterise a bigger area, several samples were taken, in the map average of these subsamples is shown. It is clearly visible that in River Zala (1) bioluminescence inhibition is very high, 72.63%. Toxicity is somewhat reduced (54.9%) at the point where the river reaches the second reservoir (2) and goes under further reduction (3). Sampling spot 4 shows high toxicity again, 69.7% and no toxicity reduction is experienced after that point (5).

One possible explanation is that agents causing sediment toxicity are mostly carried by watercourses. Contamination carried by River Zala is retained within the second reservoir, as the trend 1 → 3 shows. However, small watercourses might also pose serious risk to the system; one of them is the Hévíz-Páhoki Canal (4) and high toxicity experienced afterwards (5) can be attributed to this extra load. However, we cannot neglect the occurrence of background toxicants, so-called biochemicals, extracted from the marsh biomass (Overton et al., 1997).

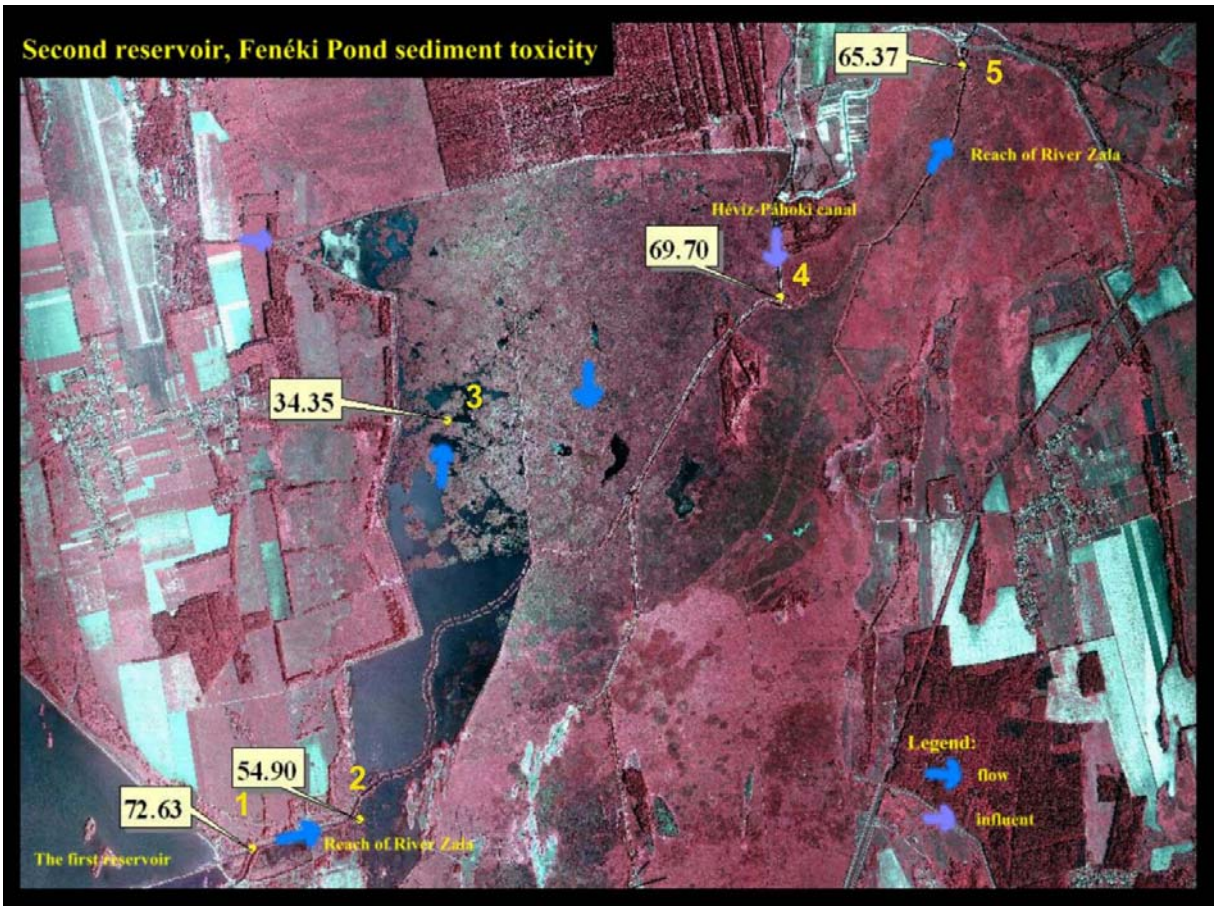

Fig.5. Sampling spots in the Kis-Balaton Water Protection System, indicating sediment toxicity measured.

4. FINAL CONCLUSIONS

Ecotoxicological tests involve several uncertainty factors (e.g. Cairns, 1993). The aim of this paper is not to discuss the inherent uncertainty of toxicity testing, rather to give guidance how to interpret toxicity values. As it was mentioned already in the introduction, establishing causality is a must if we wish to incorporate toxicity assessment in the decision making process.

The outcome of the Sós-tó case study is a risk map where both exposure and effect (toxicity) data are aggregated. Such a map is a ready-to-use tool for decision makers: not only hot spots can be identified requiring direct management measures to be taken but also, relative risk zones can be delineated.

In the case of Kis-Balaton Water Protection System, spatial distribution of toxicity data is linked to the supposed contamination sources and to the direction of contamination dilution. In this later case it is strongly emphasized that sampling and analysis should be done in an iterative manner, to distinguish background toxicity from ecological risk posed by inflow waters.

5. REFERENCES

Bennett, J., Cubbage, J. (1992). Review and Evaluation of Microtox® Test for Freshwater Sediments. Environmental Assessment Program Report, 92-e04

Bertazzon, S., Carlon, C., Critto, A., Marcomini, A., Zanetto, G. (2000). Integration of spatial analysis and ecological risk assessment in a GIS environment. The case study of the Venetian lagoon contaminated sediments. 4th International Conference on Integrating GIS and Environmental Modeling (GIS/EM4): Problems, Prospects and Research Needs. Banff, Alberta, Canada, September 2 - 8, 2000.

Burton, G. A. Jr. (1991). Assessing freshwater sediment toxicity. *Environ. Toxicol. Chem.,* **Vol. 10:** 1585-1627 pp.

Burton, G.A. Jr. (1992). Sediment Toxicity Assessment. Lewis Publishers. Boca Raton, 457 pp.

Burton, G. A. Jr., Baudo, R., Beltrami, M. and Rowland, C. (2001a). Assessing sediment contamination using six toxicity assays. *J. Limnol.*, **60 (2):** 263-267 pp.

Burton, G. A. Jr., Pitt, R. & Clark, S. (2001b). The Role of Traditional and Novel Toxicity Test Methods in Assessing Stormwater and Sediment Contamination. *Critical Reviews in Environmental Science and Technology,* **Vol. 30 (4)**

Cairns, J. (1983). Are single species toxicity tests alone adequate for estimating environmental hazard? *Hydrobiologia,* **100:** 47-57 pp.

ForEnviron Környezetvédelmi és Mérnöki Szolgáltató Kft. (2002). Koncepcióterv a székesfehérvári Sós-tó rehabilitációjához. Budapest.

Guzzella, L., Ross, P., Bartone, C. and Baudo, R. (1993). Toxicity identification evaluation of Lake Orta sediments. I SETAC World Congr. Ecotoxicology and Environmental Chemistry – a Global Perspective. Lisbon, Portugal, March 28-31, 1993. Abstract Book: abstr. 108.

Jacobs, M.W., Delfino, J.J., and Bitton, G. (1992). The Toxicity of Sulphur to Microtox® from Acetonitrile Extracts of Contaminated Sediments. *Environ. Toxicol. Chem.,* **Vol. 11:** 1137-1143 pp.

MacDonald, D. D., Ingersoll, C. G. (2002). A Guidance Manual to Support the Assessment of Contaminated Sediments in Freshwater Ecosystems. USEPA, Great Lakes National Program Office EPA-905-B02-001-C, Chicago, Illinois

Overton, E. B. Jr., Henry, C. B., Mendelssohn, I. (1997). Application of Microtox® assay to establish and evaluate the efficacy of *in situ* burning of oiled marshes. Louisiana Applied Oil Spill Research and Development Program, OSRADP Technical Report Series 96-009.

Suter, G. W. (1996). Risk Characterization for Ecological Risk Assessment of Contaminated Sites. Prepared by the Environmental Restoration Risk Assessment Program, Lockheed Martin Energy Systems, Inc., Oak Ridge, Tennessee, ES/ER/TM-200

Tátrai, I., Mátyás, K., Korponai, J., Paulovits, G., Pomogyi, P. (2000). The role of the Kis-Balaton Water Protection System in the control of water quality of Lake Balaton. *Ecological Engineering* **16:** 73-78 pp.